nature ecology & evolution

ARTICLES

https://doi.org/10.1038/s41559-020-1125-6

Check for updates

# A hydrogen-dependent geochemical analogue of primordial carbon and energy metabolism

Martina Preiner[1,8], Kensuke Igarashi[2,8], Kamila B. Muchowska[3,8], Mingquan Yu[4,8], Sreejith J. Varma[5], Karl Kleinermanns[6], Masaru K. Nobu[7], Yoichi Kamagata[7], Harun Tüysüz[4]✉, Joseph Moran[3]✉ and William F. Martin[1]✉

**Hydrogen gas, $H_2$, is generated by alkaline hydrothermal vents through an ancient geochemical process called serpentinization, in which water reacts with iron-containing minerals deep within the Earth's crust. $H_2$ is the electron donor for the most ancient and the only energy-releasing route of biological $CO_2$ fixation, the acetyl-CoA pathway. At the origin of metabolism, $CO_2$ fixation by hydrothermal $H_2$ within serpentinizing systems could have preceded and patterned biotic pathways. Here we show that three hydrothermal minerals—greigite ($Fe_3S_4$), magnetite ($Fe_3O_4$) and awaruite ($Ni_3Fe$)—catalyse the fixation of $CO_2$ with $H_2$ at 100 °C under alkaline aqueous conditions. The product spectrum includes formate (up to 200 mM), acetate (up to 100 μM), pyruvate (up to 10 μM), methanol (up to 100 μM) and methane. The results shed light on both the geochemical origin of microbial metabolism and the nature of abiotic formate and methane synthesis in modern hydrothermal vents.**

Organic synthesis in hydrothermal vents is relevant to life's origin because the reactions involve sustained energy release founded in the disequilibrium between $CO_2$ and the vast amounts of molecular hydrogen, $H_2$, generated in the Earth's crust during serpentinization[1–9]. Hydrogen has been a source of electrons and energy since there was liquid water on the early Earth, and it fuelled early anaerobic ecosystems in the Earth's crust[1,8,10]. In biochemistry, the acetyl-CoA pathway of $CO_2$ fixation uses the electrons and energy of $H_2$ to simultaneously supply three key requirements for life: reduced carbon in the form of acetyl groups, electrons in the form of reduced ferredoxin and ion gradients for energy conservation in the form of ATP[11,12]. The pathway is linear, not cyclic, it releases energy rather than requiring energy input and its enzymes are replete with primordial metal co-factors[13,14]. It traces to the last universal common ancestor[15], and abiotic, geochemical organic syntheses resembling segments of the pathway occur in modern hydrothermal vents[2,3]. Laboratory simulations of acetyl-CoA pathway reactions include the non-enzymatic synthesis of thioesters from CO and methylsulfide[16], and the synthesis of acetate[17] and pyruvate[18] from $CO_2$ using native iron or external electrochemical potentials[19] as the electron source. Enzymatic versions of those abiotic reactions occur in core energy metabolism of acetogens and methanogens[11–14], ancient anaerobic autotrophs that live from $H_2$ and $CO_2$ via the acetyl-CoA pathway and that still inhabit the crust today[14]. Although the enzymes that catalyse these modern microbial reactions have been widely investigated[11–14], catalysts promoting abiotic reactions in vents today, and that might have been instrumental at life's origin, are poorly understood[2]. A fully abiotic analogue of the acetyl-CoA pathway, from $H_2$ and $CO_2$ as it occurs in life, has not been reported to date.

To probe the mechanisms of hydrothermal metabolic reactions emulating ancient pathways, we investigated three different iron minerals that occur naturally in hydrothermal systems: greigite ($Fe_3S_4$), magnetite ($Fe_3O_4$) and the nickel iron alloy awaruite ($Ni_3Fe$). Magnetite and awaruite are common constituents of serpentinizing systems[20] and are more stable under alkaline conditions than greigite[21,22]. Magnetite, like $H_2$, is a main end product of serpentinization, being formed from water-dependent oxidation of iron(II) silicates[23]. In chemical industry, iron-based materials are the catalysts of choice for diverse industrial processes including Haber–Bosch (fixation of $N_2$) and Fischer–Tropsch syngas (CO and $H_2$) conversion to hydrocarbons[7]. Awaruite is an intermetallic compound that forms in serpentinizing systems at high-$H_2$ partial pressures and very low-$H_2S$ fugacities[5,20], via the reduction of iron(II) and nickel(II) compounds. It is common in Ni-containing serpentinizing systems, where it is usually deposited as small grains[20]. Greigite is formed under conditions of high $H_2S$ activity[5,21] as a transient intermediate in the conversion of mackinawite to pyrite[22,24]; it shares structural similarity with the iron sulfur clusters of many modern enzymes[6]. Iron sulfides can be found at the surface of hydrothermal vents either as small compartments[21] or as nanoparticles in hydrothermal plumes[25], as well as in meteorites[26]. Iron minerals have long been regarded as ancient catalysts[6,16,27], although the key initial reaction connecting the inorganic and organic world—$CO_2$ fixation with $H_2$ as the reductant—has not been reported using iron mineral catalysts under biologically relevant conditions[19].

## Results

Although very different in structure and composition (Fig. 1), greigite, magnetite and awaruite are geochemically synthesized in hydrothermal systems from pre-existing divalent iron and nickel

[1]Institute for Molecular Evolution, University of Düsseldorf, Düsseldorf, Germany. [2]Bioproduction Research Institute, National Institute of Advanced Industrial Science and Technology, Sapporo, Japan. [3]ISIS (UMR 7006), University of Strasbourg, CNRS, Strasbourg, France. [4]Max-Planck-Institut für Kohlenforschung, Mülheim an der Ruhr, Germany. [5]Charité—Universitätsmedizin Berlin, Laboratory 'Biochemistry and System Biology of the Metabolism', Berlin, Germany. [6]Institute for Physical Chemistry, University of Düsseldorf, Düsseldorf, Germany. [7]Bioproduction Research Institute, National Institute of Advanced Industrial Science and Technology, Tsukuba, Japan. [8]These authors contributed equally: Martina Preiner, Kensuke Igarashi, Kamila B. Muchowska, Mingquan Yu. ✉e-mail: tueysuez@kofo.mpg.de; moran@unistra.fr; bill@hhu.de

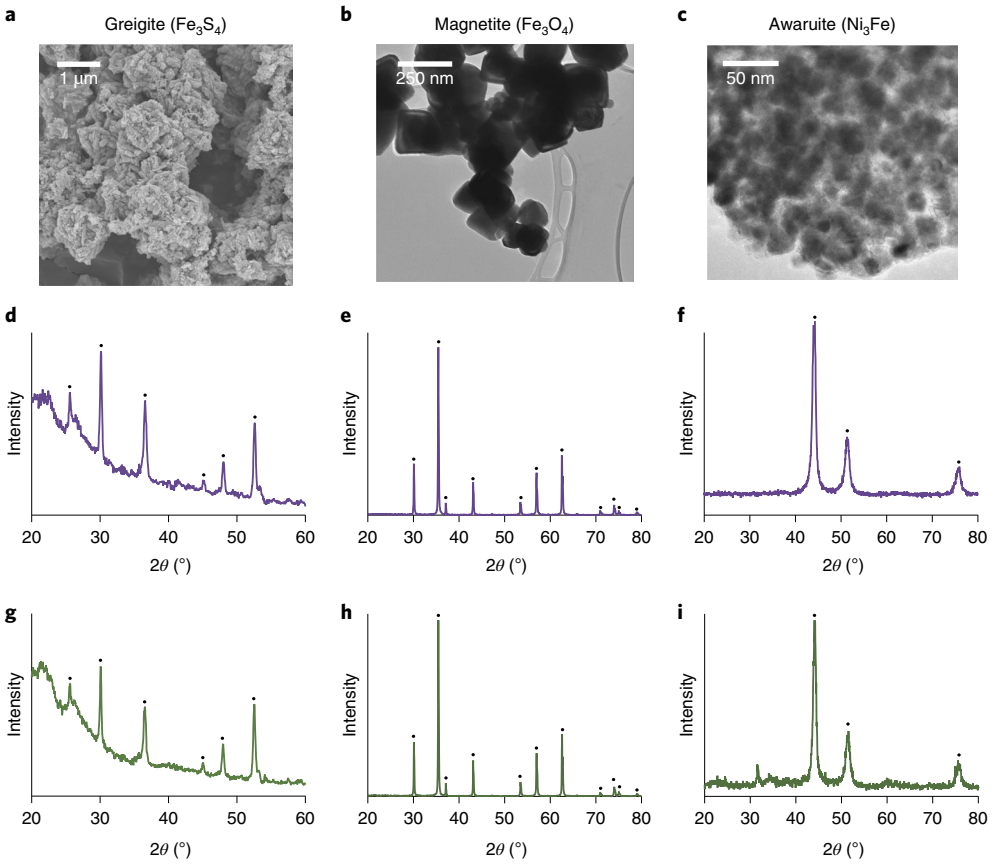


**Fig. 1 | Characterization of greigite, magnetite and awaruite catalysts. a–c**, The three powders are different in structure and morphology as seen from electron microscopy images, for which greigite (**a**) and awaruite (**c**) were freshly synthesized and magnetite (**b**) was commercially obtained. **d–i**, Comparison of XRD patterns of the minerals greigite (**d**), magnetite (**e**) and awaruite (**f**) before the reaction and after experiments under the following conditions: greigite for 24 h at pH 6.5, stabilized by a phosphate buffer under a $H_2/CO_2$ atmosphere (**g**); magnetite (**h**) and awaruite (**i**) for 16 h under alkaline conditions (KOH added) under a $H_2/CO_2$ atmosphere.

minerals during serpentinization[5,8,28]. X-ray diffraction (XRD) applied to our laboratory preparations of colloidal $Fe_3S_4$ and $Ni_3Fe$ nanoparticles (for details of synthesis, see Methods), as well as commercial $Fe_3O_4$, reveals their characteristic patterns of crystal structures (Fig. 1).

Building on evidence for catalytic reactivity in previous reports[16–19], we investigated the ability of greigite, magnetite and awaruite to promote the reduction of $CO_2$ with $H_2$ in water. Under very mild hydrothermal conditions—at 100 °C under 2 bar $H_2/CO_2$ (80/20)—formate and acetate synthesis from $H_2$ and $CO_2$ occurs readily in nearly neutral and alkaline aqueous solution in the presence of $Fe_3S_4$ (Fig. 2a). While only formate was detected at 20 °C, formate and acetate were found at 60 °C, which is close to the temperature of vent effluent (ca. 70 °C) in the Lost City hydrothermal field (Fig. 2b)[29]. At 100 bar, $Fe_3S_4$ catalyses the synthesis of formate and methane from $H_2$ and $CO_2$ (Fig. 2c), but not from CO (Extended Data Fig. 4b). Here, methane and formate production is almost stoichiometric relative to hydrogen decrease. For 14 mM $H_2$ consumed, 1 mM of formate (1 $H_2$ per molecule of formate) and 2.3 mM of methane (4 $H_2$ per molecule of methane) are produced, leaving only 3.8 mM of $H_2$ that might be available for acetate synthesis (which was below detection level in this experimental set-up). At 2 bar, formate accumulates to >2 mM within 4 h while the detection of acetate requires 4–8 h (Fig. 2d). Notably, formate and methane are the main products of abiotic organic synthesis observed in the effluent of modern serpentinizing hydrothermal systems[9,30–33].

We found that magnetite, like greigite, catalyses the aqueous synthesis of formate and acetate in the range of 10 µM to 1 mM from $H_2$ and $CO_2$, but also the formation of methanol and pyruvate under mild (25 bar $H_2/CO_2$, 40/60 ratio and 100 °C) hydrothermal conditions (Fig. 3a). Pyruvate is a crucial intermediate of carbon and energy metabolism in nearly all microbes, and the main product of $CO_2$ fixation in autotrophs that use the acetyl-CoA pathway[11]. It accumulates at 5–10 µM in the presence of $Fe_3O_4$ across the pH range 6.0–10.0, when either native iron (Fe) or $H_2$ is used as the reductant (Fig. 3a). Magnetite generates a generally uniform product distribution across conditions tested, and also when smaller amounts of catalyst are used (Extended Data Fig. 6b). Additionally we investigated different amounts of Fe as a reductant, showing that its impact on product concentrations is low even when a large excess of Fe was used. Both Fe and $Fe_3O_4$ formed a solid disc after the reaction, which probably hindered further oxidation of Fe and thus further accumulation of reduced carbon compounds (Extended Data Fig. 7a).

At 100 °C, awaruite catalyses the synthesis of acetate and methanol in the range 10–100 µM at pH 5.0–8.0 whereby either the native alloy itself, $H_2$ or native Fe can function as the reductant, albeit with differing efficiency and product distribution (Fig. 3b). Under alkaline conditions, with either native Fe or $H_2$ as reductant, formate accumulates in the 200 mM range with 1 mmol of metal atoms as catalyst. Physical contact between awaruite and native iron is not required for product formation (Extended Data Fig. 7b). In the case of awaruite, lower temperatures improved pyruvate synthesis (Fig. 4a), similar to previous studies[18]. Pyruvate is formed under alkaline

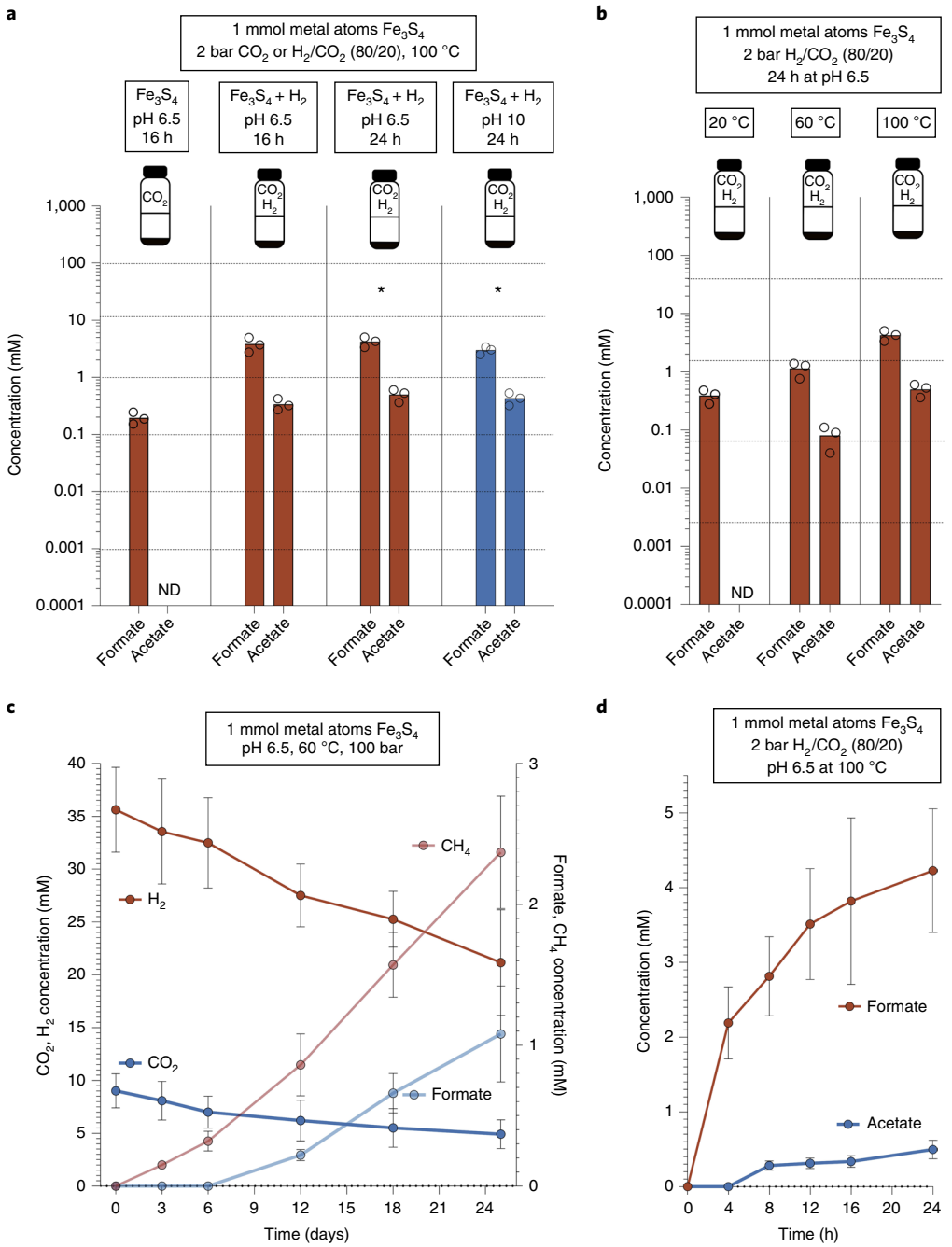


**Fig. 2 | Fixation of $CO_2$ with $H_2$, catalysed by greigite. a**, Catalysis by greigite at 100 °C. **b**, Effect of temperature on greigite catalysis. **c**, Time course experiment of high-pressure methane and formate production from $CO_2$ and $H_2$ under greigite catalysis (liquid phase, 150 ml) at 100 bar and 60 °C. **d**, Reaction progress over time under a 2-bar $H_2/CO_2$ atmosphere and 100 °C. All reactions were performed in water containing a phosphate buffer (**a**,**b**,**d**, 3 ml, **c**, 150 ml). **a**,**b**, Flasks summarize the reaction parameters, with greigite depicted in black. Amounts of catalyst are normalized by the number of moles of metal atoms per mole of mineral compound: 0.33 mmol of greigite is equivalent to 1 mmol of metal atoms in each catalyst. Individual experiments were performed under either $CO_2$ or $H_2/CO_2$ atmosphere. Red bars, pH < 7.0; blue bars, pH > 7.0. ND, not detected (no product was formed, or product concentration was below the detection limit). Circles correspond to the values of individual experiments. Values of 0 are not shown on the logarithmic scale. Asterisks indicate experiments for which Gibbs free energy was calculated in Table 1. Experimental concentration values and s.d. are listed in Supplementary Table 1, and control experiments are shown in Extended Data Fig. 2a. The influence of pH (4.0–10.0) on reactions catalysed by greigite is shown in Extended Data Fig. 4a.

conditions at 70 °C (Fig. 4a), even at lower amounts of catalyst than previously used (0.5 mmol of metal atoms), and reaches 10 µM when higher amounts are used (Fig. 4b). This suggests that pyruvate production in reactions with smaller amounts of awaruite probably occurs, but is below the detection limit of the $^1$H-nuclear magnetic resonance (NMR) spectroscopy used here. Using even less $Ni_3Fe$ (0.05 mmol metal atoms) is still effective for formate, acetate and methanol formation in thermal gradients from 100 to 30 °C (Extended Data Fig. 6a,c), conditions similar to those of natural alkaline hydrothermal vents[29]. Catalysts are required for the

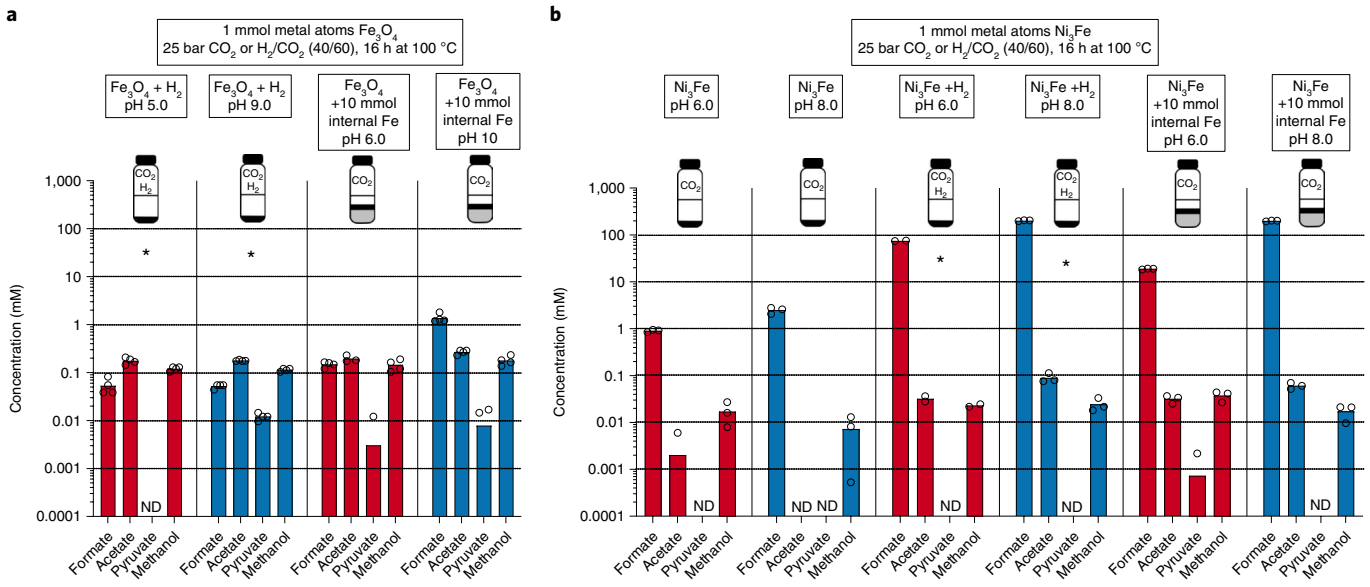


**Fig. 3 | Fixation of $CO_2$ with $H_2$, catalysed by magnetite and awaruite. a**,**b**, Catalysis by magnetite (**a**) and awaruite (**b**). All reactions were performed in water (1 ml). Flasks in each panel summarize the reaction parameters: hydrothermal minerals are depicted in black, additional iron powder in grey. Amounts of catalyst are normalized by the number of moles of metal atoms per mole of mineral compound: 0.33 mmol of magnetite, as well as 0.25 mmol of awaruite, are equivalent to 1 mmol of metal atoms in each catalyst. Individual experiments were performed under either $CO_2$ atmosphere, $H_2/CO_2$ atmosphere or $CO_2$ atmosphere with Fe powder as an electron source (also for $H_2$ formation from $H_2O$). Experiments without native Fe were performed with decontaminated stir bars; those containing native Fe were performed without stir bars due to solidification of Fe powder during the process. Red bars, pH < 7.0; blue bars, pH > 7.0. ND, not detected (no product was formed, or product concentration was below the detection limit). Experiments performed at pH < 7.0 were treated with KOH after the reaction, as in Varma et al.[18]. Circles correspond to the values of individual experiments. Values of 0 are not shown on the logarithmic scale. Asterisks indicate experiments for which Gibbs free energy was calculated in Table 1. Concentration values and s.d. of the experiments are listed in Supplementary Table 1, and control experiments are shown in Extended Data Figs. 2b,c (awaruite) and 3 ($Fe^0$) and Supplementary Tables 4–7. Background levels of formate at least three orders of magnitude below experimental product concentrations (awaruite); background levels of acetate (ca. 10–20 μM) were observed in controls using awaruite as catalyst. All background levels were subtracted before plotting (see Supplementary Information for all background values).

reaction—controls without catalysts yielded only trace levels of product (Extended Data Fig. 2b,c and Supplementary Tables 6 and 7).

In some experiments using $Ni_3Fe$, we detected ethanol in concentrations up to >100 μM (Extended Data Fig. 5b). We observed trace amounts of methane (ca. 19 ppm) in awaruite-catalysed reactions (Extended Data Fig. 8), which is substantially less than that detected in an earlier report using $H_2$ and $CO_2$ for 1–2 weeks at 500 bar and 200–400 °C with awaruite as the catalyst[34]. The hydrothermal conditions we found for the synthesis of organics from $H_2$ and $CO_2$ over 16 h with awaruite as catalyst are sufficiently mild in terms of temperature and energetics to permit microbial growth. Of the catalysts employed, only awaruite showed minor alteration after reaction, probably due to mild oxidation (Fig. 1g–i). Formate accumulation catalysed by awaruite reflects the near-equilibrium interconversion of $H_2$–$CO_2$ and formate[35].

To avoid contamination, no organic buffers were employed in any of our experiments. Because greigite is sensitive to high pH, phosphate buffer was employed here. In the experiments with magnetite and awaruite, no buffers were used. In Figs. 3 and 4, blue bars indicate reactions where the starting pH was ~11.0 through the addition of KOH to generate alkaline vent conditions; the pH measured at completion is dependent on the amount of mineral used and metal, in addition to the amount of $CO_2$ dissolved and organic acid synthesized. No water loss, which would potentially distort the product concentrations, was detected in any of our experiments.

Sustained synthesis of reactive organic compounds was essential at the origin of metabolism and had to be thermodynamically favourable. Equations (1–5) show the redox reactions taking place between $CO_2$ and $H_2$ to form formate (equation (1)), methanol (equation (2)), acetate (equation (3)), pyruvate (equation (4)) and methane (equation (5)).

**Table 1 | $\Delta G$ for $CO_2$ fixation product formation (kJ $mol^{-1}$)**

| | Greigite | | Magnetite | | Awaruite | |
|---|---|---|---|---|---|---|
| **Product** | **1** | **2** | **3** | **4** | **5** | **6** |
| Formate | 0.31 | −25.58 | −19.56 | −48.14 | −2.56 | −15.26 |
| Methanol | ND | ND | −46.60 | −46.60 | −51.49 | −50.33 |
| Acetate | −71.00 | −96.69 | −108.59 | −137.16 | −120.03 | −132.17 |
| Pyruvate | ND | ND | ND | −57.18 | ND | ND |

Values of $\Delta G$ refer to the reactions as shown in equations (1–5). The conditions are those for reactions marked with asterisks in Figs. 2 and 3. Details of reaction conditions for columns 1–6: (1) 0.33 mmol $Fe_3S_4$, 100 °C, 24 h, pH 6.5, 2 bar $H_2/CO_2$ (80/20); (2) 0.33 mmol $Fe_3S_4$, 100 °C, 24 h, pH 10.0, 2 bar $H_2/CO_2$ (80/20); (3) 0.33 mmol, $Fe_3O_4$, 100 °C, 16 h, pH 6.0, 25 bar $H_2/CO_2$ (40/60); (4) 0.33 mmol, $Fe_3O_4$, 100 °C, 16 h, pH 9.0, 25 bar $H_2/CO_2$ (40/60); (5) 0.25 mmol, $Ni_3Fe$, 100 °C, 16 h, pH 6.0, 25 bar $H_2/CO_2$ (40/60); (6) 0.25 mmol, $Ni_3Fe$, 100 °C, 16 h, pH 8.0, 25 bar $H_2/CO_2$ (40/60). Columns 1, 3, 5: pH < 7.0; columns 2, 4, 6: pH > 8.0. ND, not detected (no product was formed or product concentration was below the detection limit). Values of $\Delta G$ for product accumulation at 100 nM in these experiments (below the detection level) are given in Supplementary Table 3.

$$H_2 + CO_2 \rightarrow HCOO^- + H^+ \quad (1)$$

$$3H_2 + CO_2 \rightarrow CH_3OH + H_2O \quad (2)$$

$$4H_2 + 2CO_2 \rightarrow CH_3COO^- + 2H_2O + H^+ \quad (3)$$

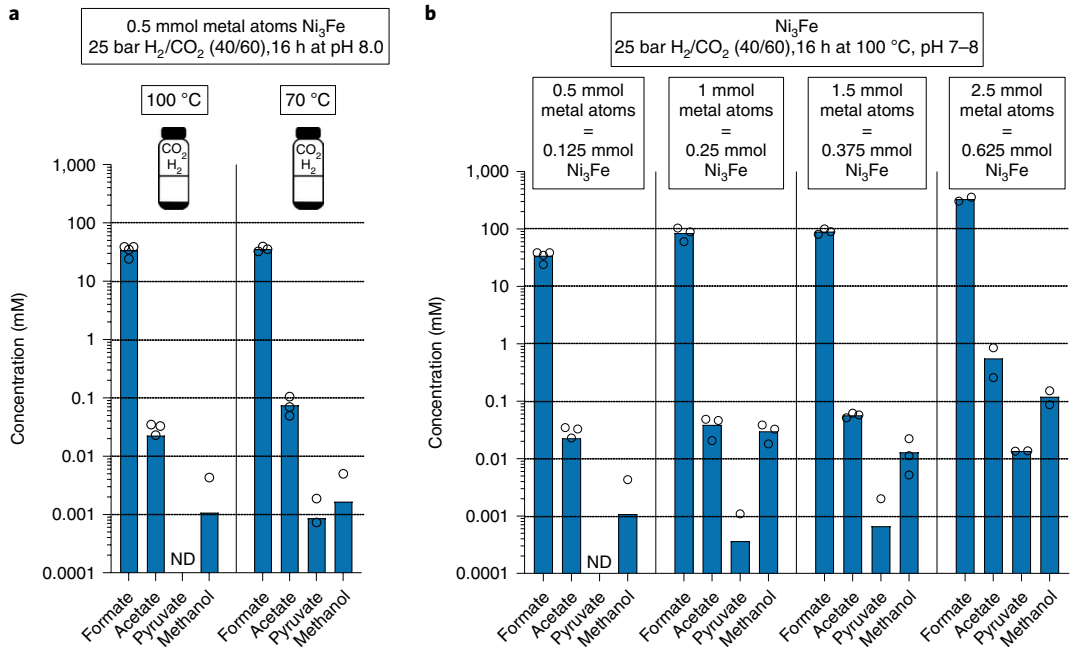


**Fig. 4 | Awaruite catalyses synthesis of formate, acetate, and pyruvate. a**, Effect of temperature on awaruite catalysis. **b**, Impact of amount of awaruite catalyst used. All reactions were performed in water (1 ml). Amounts of catalyst used are normalized to the number of moles of metal atoms per mole of mineral compound: 0.25 mmol of awaruite is equivalent to 1 mmol of metal atoms. Individual experiments were performed under $H_2/CO_2$ (40/60) atmosphere. All experiments were conducted without stir bars. Values of 0 are not shown on the logarithmic scale. All measurements were performed in at least triplicate (2.5 mmol of awaruite in duplicate). ND, not detected (no product was formed or product concentration was below the detection limit). Circles correspond to values obtained in individual experiments. Experimental concentration values and s.d. are listed in Supplementary Table 1, and control experiments are shown in Extended Data Fig. 2b,c and Supplementary Tables 6 and 7.

$$5H_2 + 3CO_2 \rightarrow CH_3(CO)COO^- + 3H_2O + H^+ \quad (4)$$

$$4H_2 + CO_2 \rightarrow CH_4 + 2H_2O \quad (5)$$

The changes in Gibbs free energy, $\Delta G$, for six of the $H_2$-dependent reactions reported here are given in Table 1 (detailed datasets are shown in Supplementary Tables 2 and 3). The synthesis of observed products is close to equilibrium or exergonic. For most compounds and conditions, product generation did not reach equilibrium, indicating the kinetic inhibition of reactions. Only $H_2$-dependent reduction of $CO_2$ to formate approached equilibrium in the presence of greigite or awaruite (according to experiments in Figs. 2a and 3b). Pyruvate and $CH_4$ production were detected only under specific conditions despite being exergonic in nearly all treatments. In treatments with $H_2$ and magnetite, for example, pyruvate generation was detected only under alkaline conditions (Fig. 3a), while in treatments with $H_2$ and awaruite it was detected only under alkaline conditions and when the amount of mineral was increased (Fig. 4b). $H_2$-dependent reduction of formate to acetate (equation (3) – equation (1)); $3H_2 + CHOO^- + CO_2 \rightarrow CH_3COO^- + 2H_2O$) consistently reached similar $\Delta G$ values for each mineral, regardless of pH and mineral content (approximately −72, −89 and −115 kJ mol$^{-1}$ at 100 °C for greigite, magnetite and awaruite, respectively), suggesting the possibility of shared features between the minerals' catalytic mechanisms. None of the three minerals catalysed acetate synthesis to completion ($\Delta G << 0$), suggesting the possible presence of kinetic barriers and an opportunity for energetic coupling. For those reactions in which no $H_2$ was added, only native metals were available as reductant (Extended Data Figs. 3, 5a and 7), probably generating intermediate $H_2$ from water.

## Discussion

When greigite, magnetite or awaruite is used as a catalyst, the synthesis of formate, acetate, methanol and pyruvate from $H_2$ and $CO_2$ under hydrothermal conditions is facile. The synthesis of formate and acetate is furthermore robust to the catalyst employed. The main product we observed was formate (Figs. 2–4), which is also the main organic product of abiotic organic synthesis found in alkaline hydrothermal vent effluent[9,31,36,37]. We propose a mechanism for the catalysed two-electron reduction of $CO_2$ to formate for all three minerals (Extended Data Fig. 10).

Formate synthesis from $H_2$ and $CO_2$ was anticipated by earlier studies[38,39], and formate synthesis from $CO_2$ has been reported at high temperatures (> 250 °C) and pressures (> 300 bar) with hydrothermal minerals[40]. However, the amounts of formate we observed with $Ni_3Fe$ at moderate temperature and pressure (70–100 °C and 25 bar $H_2/CO_2$ atmosphere), as well as the accumulation of acetate and pyruvate, reveal an unexpected correspondence between spontaneous $H_2$-dependent $CO_2$ reduction and metabolism. We see a clear tendency of Ni-containing compounds to preferentially produce formate in high concentrations[18], while pyruvate accumulation is preferentially observed with Fe. These product-catalyst specificities are reflected in the active site metals of corresponding enzymes of the modern acetyl-CoA pathway[11–13,41–46].

Under physiological conditions, the reducing power of $H_2$ is insufficient to reduce $CO_2$. Microbes studied to date reduce $CO_2$ with electrons from $H_2$, employing flavin-based electron bifurcation to synthesize reduced iron sulfur clusters in ferredoxin for $CO_2$ fixation[12,47]. This biological $CO_2$ fixation usually also entails ion gradients[47,48]. The reactions reported here require neither electron bifurcation nor ion gradients. With suitable inorganic catalysts that activate both $H_2$ and $CO_2$ to enable their reaction, products of the

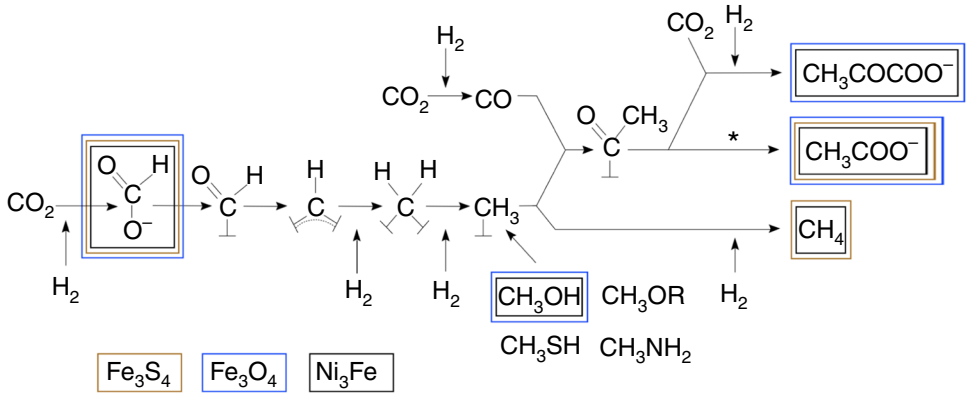


**Fig. 5 | Congruence between the acetyl-CoA pathway and reactions catalysed by three iron minerals found in hydrothermal vents.** The chemical reactions shown summarize the acetyl-CoA pathway as it occurs in hydrogenotrophic bacteria and archaea, as depicted in ref. [11], with the exception of free formate later discovered in the archaeal pathway[65]. The methenyl (=CH-), methylene (-$CH_2$-) and methyl (-$CH_3$) groups of the bacterial and archaeal pathways are bound to tetrahydrofolate and tetrahydromethanopterin, respectively, generically indicated here as catalysts (⊥). Colour-edged boxes indicate products observed in reactions using iron mineral catalysts. Asterisk indicates the reaction sequence in which energy is conserved as ATP via substrate-level phosphorylation in the biological pathway (acyl-nickel, thioester and acyl-phosphate intermediates employed by the enzymatic pathway for stepwise conservation of free energy in exergonic conversion of the nickel-bound acyl group to ATP[11] are not shown). All products shown were observed at temperatures ≤ 100 °C and obtained within < 24 h, except methane in the case of greigite, which was observed over the course of 25 d (Fig. 2c). Methanol, methyl sulfide, methyl amines and methoxy groups from coal can serve as methyl donors for the pathway[11,66].

acetyl-CoA pathway (Figs. 2, 3 and 4) are formed without the addition of organic co-factors.

With the exception of ethanol, the reaction products we observe correspond exactly to those of the biological acetyl-CoA pathway to pyruvate[11] (Fig. 5). No other reaction products were observed. That is, the mineral-catalysed $H_2$-dependent reduction of $CO_2$ delivers a very discrete subset of possible chemical structures: one that constructs the backbone of carbon and energy metabolism in primitive anaerobic autotrophs[11–15]. The acetyl-CoA pathway[11,14] entails 11 main enzymes totalling ~15,000 amino acid residues[13,41–45] plus six organic co-factors, each with its own complex biosynthesis[14]. The bacterial and archaeal versions of the pathway involve evolutionarily unrelated enzymes but chemically similar methyl synthesis routes[6,11,14]. The reactions of the acetyl-CoA pathway employed in modern metabolism (Fig. 5) involve the stepwise conservation of chemical energy during $CO_2$ fixation as acetyl-nickel, acetyl-thioester, acetyl-phosphate and ATP synthesis via substrate-level phosphorylation (marked with an asterisk in Fig. 5)[11–14]. Although the nature of catalyst-bound intermediates of the biological pathway from $H_2$ and $CO_2$ to methane, acetate and pyruvate is known[11–14], the identity of catalyst-bound intermediates of mineral-catalysed reactions is not.

Proposals for the nature of primordial $CO_2$ fixation and energy conservation at biochemical origins typically posit the participation of external energy sources[49], such as UV light[50], heat, impact, pressure, electrical currents or ion gradients[28], to push organic synthesis forward. The reactions reported here require no additional energy source for the unfolding of a protometabolic acetyl-CoA pathway from $H_2$ and $CO_2$ other than the natural reactivity of two gases and metal catalysts, indicating that neither membranes, though essential for the emergence of free-living cells[6,51–53], nor external potentials[19,54] were required for primordial $CO_2$ fixation along an exergonic, $H_2$-dependent, non-enzymatic pathway to C3 products. The energy for the synthesis of compounds capable of phosphorylating ADP via substrate-level phosphorylation[6,11,12]—for reactions reported here, and for those of the enzymatically catalysed acetyl-CoA pathway—stems from the exergonic synthesis of biologically relevant organic compounds from $H_2$ and $CO_2$. Our findings suggest that abiotic, geochemical versions of energy-releasing reactions underlying the acetyl-CoA pathway very likely preceded the enzymes that catalyse it today[11,14,18,55]. The simplicity and primordial nature of these reactions furthermore suggests that metabolism elsewhere could initiate by a similar route.

## Methods

**General information.** An overview of the experiments performed can be found in Extended Data Fig. 1, and relevant controls in Extended Data Figs. 2 and 3 and Supplementary Tables 4–7. The quantity of each transition metal reagent tested as a carbon fixation catalyst was normalized so that it would contain the same number of millimoles of metal atoms across the experiments. For example, 1 mmol of metal atoms corresponds to 0.33 mmol of greigite (99 mg), 0.33 mmol of magnetite (77 mg) and 0.25 mmol of awaruite (58 mg). Each reaction was performed in at least triplicate. Information on suppliers, grade and purity of all reagents used is listed in the Supplementary Information.

**Synthesis of greigite.** Every piece of apparatus used in greigite synthesis was stored in an anaerobic chamber (Coy Laboratory Products) under a gas mixture of $N_2$/$H_2$/$CO_2$ (80/5/15) for at least 48 h before use, to remove residual oxygen. Reagents for greigite synthesis were purged with $N_2$ before use unless otherwise stated. Amorphous FeO(OH) was synthesized as reported previously[56] and suspended in Milli-Q water (0.30 mol $l^{-1}$) under air atmosphere. After purging with $N_2$, this suspension was stored in a glass bottle under $N_2$/$H_2$/$CO_2$ (80/5/15). Solutions of $Na_2S$ (1.0 M) and $H_2SO_4$ (2.0 M) were prepared as reported previously[57] and stored in a glass bottle under $N_2$. Greigite was synthesized in a solid–gas reaction system as reported previously[57] with slight modifications. In brief, amorphous FeO(OH) (0.66 mmol, 2.2 ml of water suspension) was aliquoted to a glass reaction vessel, and a test tube containing 1.0 ml of the $Na_2S$ solution was placed in the vessel inside the anaerobic chamber. The vessel was sealed with an ethylene tetrafluoroethylene (ETFE)-coated butyl rubber stopper and an aluminium seal. The vessel was then removed from the anaerobic chamber and the headspace gas replaced with Ar. After returning the vessel to the anaerobic chamber, $H_2S$ gas was generated inside the vessel by injecting 0.5 ml of the $H_2SO_4$ solution into the $Na_2S$ solution in the test tube using a disposable Myjector syringe (Terumo). The vessel was incubated at 80 °C for 3 h. The resulting greigite suspension was collected by pipetting from several reaction vessels, washed with 0.5 M HCl and then rinsed with $N_2$-purged Milli-Q water in the anaerobic chamber as described previously[57].

**$CO_2$ fixation catalysed by greigite.** Synthesized greigite (0.33 mmol) was resuspended in 3 ml of potassium phosphate buffer (20 mM) of designated pH. The greigite suspension was placed in a fresh glass reaction vessel, which was then sealed with an ETFE-coated butyl rubber stopper and an aluminium seal. The vessel was then removed from the chamber and the headspace gas replaced with $H_2$/$CO_2$ (80/20) or $CO_2$ outside the chamber. Vessels were incubated at 100 °C over 4–24 h.

**High-performance liquid chromatography (HPLC) analysis (greigite experiments).** Liquid-phase components were analysed on a D-2000 LaChrom

Elite HPLC system (Hitachi), equipped with an Aminex HPX-87H column (300 mm, 7.8 mm internal diameter (i.d.); Bio-Rad Laboratories) and an L-2400 UV detector at 240 nm and L-2490 RI detector as described previously[58]. Supernatants obtained in the $CO_2$ reduction experiments were collected after centrifugation inside the anaerobic chamber, then 10 µl of the supernatants obtained were directly injected into the HPLC circuit and chromatographed under an isocratic flow of 0.7 ml $min^{-1}$ (eluent, 10 mM $H_2SO_4$ in $H_2O$). Column temperature was maintained at 50 °C. Identities of the analytes detected were determined by the liquid chromatography–tandem mass spectrometry system: Agilent 1200 HPLC (Agilent Technologies) coupled to an HCT Ultra mass spectrometer (Bruker Daltonics) using a Shodex HILICpak VG-50 2D column (150 mm, 2 mm i.d.; Showa Denko). The supernatant prepared as above was mixed with an equal amount of the eluent, then 5 µl of the mixture was injected into the HPLC circuit and chromatographed under an isocratic flow of 0.1 ml $min^{-1}$ (eluent, a mixture of acetonitrile and 0.25% ammonia water at 80/20). Column temperature was maintained at 30 °C.

**High-pressure measurements (greigite experiments).** A previously developed[59] high-pressure incubation system was used for the high-pressure $CO_2$ (Fig. 2c) and CO (Extended Data Fig. 4b) reduction reactions in this study. The system consisted of an incubation vessel (stainless steel with Sulfinert coating on its internal wall, volume 150 $cm^3$; Swagelok), inflow/outflow tubes with valves (Swagelok) and a 500D automated syringe pump (Teledyne Isco). Greigite suspension was placed in the reaction vessel inside the anaerobic chamber. After sealing the vessel with inflow and outflow tubes, the headspace gas was replaced with $H_2 + CO_2$ (80/20) through a rubber septum equipped with an inflow tube, via a needle. This vessel was then connected to the syringe pump via the inflow tube to complete the incubation system. Potassium phosphate buffer was injected by the syringe pump to reach a hydrostatic pressure of 100 bar. Incubation at 60 °C started after $H_2$ and $CO_2$ were completely dissolved in the liquid phase (verified by gas chromatography analysis). Samples were periodically collected via the outflow tube while keeping the same hydrostatic pressure through automated pressure control of the syringe pump.

**Gas analysis (greigite experiments).** Gas-phase measurements were carried out on a gas chromatograph GC-2014 (Shimadzu) as described previously[58]. Depending on the target gas component, different columns and detectors were used: an Rt-QPLOT (30 m, 0.32 mm i.d., 10 µm F.T.; Restek) with flame ionization detector (FID) for $CH_4$, molecular sieve 13× column (2 m, 3 mm i.d.; Shimadzu) with a thermal conductivity detector (TCD) for $H_2$ and CO, and activated charcoal column (2.0 m, 3 mm, 60/80 mesh; Shinwa Chemical Industries) with TCD for $CO_2$. Pure He and Ar were used as carrier gases for FID and TCD, respectively. Gases were identified by gas chromatography–mass spectrometry (GC–MS) using two systems: (1) TQ8040 NX GC–MS (Shimadzu) equipped with a polar capillary column (TC-70, 30 m, 0.25 mm i.d., 0.25 µm F.T.; GL Sciences); (2) QP2010 Plus GC–MS (Shimadzu) equipped with Rt-Q-BOND (15 m, 0.32 mm i.d., 10 µm F.T.; Restek). Carrier gas in both systems was pure He.

**Synthesis of awaruite ($Ni_3Fe$) nanoparticles.** As previously reported[60,61], spent tea leaves can be used as sustainable hard template to synthesize native metal nanoparticles at the desired composition. For the synthesis of nanoparticular $Ni_3Fe$, washed and dried tea leaves were added to an aqueous solution of $Ni(NO_3)_2{\cdot}6H_2O$ and $Fe(NO_3)_3{\cdot}9H_2O$ (molar ratio 3/1) and stirred at room temperature for 2 h. The mass ratio of tea leaves and metal precursors was set at 2/1. Due to the low decomposition temperature of the metal nitrate salt (< 200 °C), metal oxide nanoparticles can be formed in the pore confinement of the template before its structural damage/combustion. The carbon-based tea leaf template was burned out in air atmosphere (550 °C for 4 h), and the resulting $Ni_3Fe$ oxide was washed with 0.1 M HCl solution for 2 h and cleaned with deionized water. Finally, the product was treated in a reductive 10% $H_2$/Ar flow (100 ml $min^{-1}$) at 500 °C for 2 h to generate the intermetallic $Ni_3Fe$ compound.

**$CO_2$ fixation catalysed by magnetite and awaruite.** Awaruite and magnetite powders (commercial) were placed in a 1.5-ml glass vial. In the case of the magnetite and awaruite experiments shown in Fig. 3, a clean polytetrafluoroethylene (PTFE)-coated stir bar was added to the vial. All further awaruite experiments were conducted without stir bars. The reaction vials were then filled with 1.0 ml of Milli-Q water. Whenever the effect of increased pH of the reaction mixtures was tested, solid KOH was added to Milli-Q water before the reaction (45 mg $ml^{-1}$). KOH had previously been tested for contaminants by $^1$H-NMR analysis (Extended Data Fig. 9a). To prevent cross-contamination while allowing for ready access of the gas to the reaction mixture, the vials were closed by caps with punctured PTFE septa. The reaction vials (3–12) were placed in a stainless-steel pressure reactor (Berghof or Parr) which was then sealed, flushed three times with ca. 5 bar $CO_2$, pressurized to a final value of 25 bar $CO_2$ (unless noted otherwise) and heated at the desired temperature (an external heating mantle was used) for 16 h. At a reaction temperature of 100 °C, a maximum pressure of ca. 30 bar was reached. After the reaction, the reactor was allowed to cool to room temperature (3–4 h from 100 °C, 2–3 h from 70 °C) before sample analysis[18,55].

**Experiments with iron powder or hydrogen gas.** These experiments were performed according to the general procedure described above, except that 10 mmol (560 mg) of $Fe^0$ powder was first placed in the reaction vials followed by the mineral tested and no stir bars were added. Further experiments exploring the impact of the amount of $Fe^0$ powder are shown in Extended Data Fig. 7a. Whenever $H_2$ was used in the experiments, the pressure reactor was first flushed with $CO_2$, pressurized with 10 bar of $H_2$ and then brought to 25 bar by further addition of $CO_2$ ($H_2/CO_2$ approximately 40/60).

**Work-up procedure for reaction mixtures (magnetite and awaruite).** The pH of individual reaction mixtures was determined via TRITEST L pH 1.0–11.0 papers (Macherey-Nagel) directly after the reaction. The values of $Ni_3Fe$ experiments were confirmed with a pH metre (Lab 875, SI Analytics) and a pH combination micro-electrode (A 157 IDS, SI Analytics). $CO_2$ dissolved in the reaction mixture during the reaction decreased reaction pH values due to the formation of carbonic acid. Reaction mixtures that did not contain KOH were either treated with ca. 45 mg of solid KOH per 1-ml reaction mixture to precipitate the metal ions as hydroxides (in the case of $Fe_3O_4$ and $Ni_3Fe$ experiments, shown in Fig. 3), or left untreated (in the case of $Ni_3Fe$). The treatment of individual experimental rows was also dependent on the visible concentration of metal ions in solution (since these ions have to be removed by precipitation as hydroxides before NMR measurements), and is additionally described in the corresponding figure legends. All samples were then centrifuged at 13,000 r.p.m. for 10 min. The supernatant was then separated from the precipitate (catalyst) and stored at 4 °C overnight or longer before NMR or HPLC analysis.

**NMR analysis (magnetite and awaruite).** Concentrations of formate, acetate, pyruvate and methanol (as methoxide) were determined by $^1$H-NMR, following the protocol established in Varma et al.[18]. The supernatant of the centrifuged samples was mixed with sodium 3-(trimethylsilyl)-1-propanesulfonate $D_2O$-solution as the internal standard ($CH_3$ peak at 0 ppm). NMR spectra were acquired on either a Bruker Avance III 600 or 300 spectrometer at 297 K, using a ZGESGP pulse programme. Thirty-two scans were acquired for each sample and the relaxation delay was set to 40 s (600 MHz) and 87 s (300 MHz), with a spectral width of either 12,315 ppm (600 MHz) or 11,963 ppm (300 MHz). Analysis and integration were performed using MestReNova (v.10.0.2) software. Shifts of the measured products are depicted in Extended Data Fig. 9b.

**Powder X-ray diffraction.** Power XRD analysis was performed for pre- and post-reaction catalysts. For greigite, XRD specimes were prepared as described previously[57]. In brief, sampls were collected by centrifugation and the pellet obtained directly mounted in slurry form on a silicon holder (SanyuShoko), then sealed using polyimide film (Nilaco Corporation) and vacuum grease (JEOL) to avoid possible desiccation and oxidation during analysis. Specimens were analysed using a RINT2000 X-ray diffractometer (Rigaku) at room temperature for $CuK\alpha_{1,2}$ radiation scanning at a step interval of 0.02° 2$\theta$ and a counting time of 2 s with a 2$\theta$ range of 20–60°, operating at an accelerating voltage of 40 kV at 30 mA. To prepare specimens for magnetite and awaruite experiments, samples were collected, washed with Milli-Q water and dried under vacuum. XRD patterns of these specimens were collected at room temperature using a theta-theta diffractometer (Stoe) in BraggBrentano geometry for $CuK\alpha_{1,2}$ radiation scanning, at a step interval of 0.04° 2$\theta$ and a counting time of 6 s with a 2$\theta$ range of 20–80°.

**Electron microscopy.** Electron microscopic observation was conducted for pre-reaction catalysts to check their morphology. For greigite, specimens were prepared as described previously[57]. Briefly, in the anaerobic chamber, greigite was rinsed at least three times with $N_2$-purged Milli-Q water, dried at room temperature and then mounted on an aluminium stab using carbon tape. Specimens were removed from the anaerobic chamber, coated with platinum/palladium alloy with an ion-sputter E102 (Hitachi) and observed on either a JSM-6330F (JEOL) or JSM-7800F (JEOL) field-emission scanning electron microscope at an acceleration voltage of 5 kV. Magnetite samples were deposited on lacy carbon film-coated Cu grids (400 mesh) and observed on an H-7100 (Hitachi) transmission electron microscope at an acceleration voltage of 100 kV. Awaruite samples were collected and embedded in Spurr resin (hard mixture). Resin blocks thus obtained were trimmed using an EM TRIM milling system (Leica). Thin sections were cut from the resin blocks by microtome with a 35° diamond knife (Reichert Ultra-Cut), dispersed in Milli-Q water, transferred from the water surface on lacy carbon film-coated Cu grids (400 mesh) and observed on an S-5500 (Hitachi) scanning transmission electron microscope at an acceleration voltage of 30 kV.

**Thermodynamic calculations.** For $\Delta G$ calculations, published values of $\Delta H$ (reaction enthalpy) and $\Delta G$ values were used[62,63]. The effect of temperature on Gibbs free energy yield was calculated using the Gibbs–Helmholtz equation. Equilibrium constants at different temperatures were adjusted using the van't Hoff equation (detailed equations given in Supplementary Information). Corrections based on non-standard pressures were estimated using partial molar volume changes of the reactions[64]. For any organic compounds not detected, an aqueous concentration of 0.1 µM was assumed. For $CH_4$, a partial pressure of $10^{-7}$ bar was

assumed when not detected. In reactions containing $Fe^0$ as an electron donor (Supplementary Table 2), $H_2$ concentration was estimated by assuming that $H_2$-dependent $CO_2$ reduction to formate reached equilibrium. Final $H_2$ and $CO_2$ concentrations were estimated based on the measured products (subtracting 1 mol of $H_2$ per mole formate detected).

**Reporting Summary.** Further information on research design is available in the Nature Research Reporting Summary linked to this article.

## Data availability

All data are available in the main text, Extended Data Figs. 1–10 and the Supplementary Information (Supplementary Methods, Supplementary Tables 1–7, Supplementary Figs. 1–29 and Supplementary Equations).

Received: 9 July 2019; Accepted: 23 January 2020;
Published online: 02 March 2020

## References

1. Baross, J. A. & Hoffman, S. E. Submarine hydrothermal vents and associated gradient environments as sites for the origin and evolution of life. *Orig. Life Evol. Biosph.* **15**, 327–345 (1985).
2. McCollom, T. M. Abiotic methane formation during experimental serpentinization of olivine. *Proc. Natl Acad. Sci. USA* **113**, 13965–13970 (2016).
3. McDermott, J. M., Seewald, J. S., German, C. R. & Sylva, S. P. Pathways for abiotic organic synthesis at submarine hydrothermal fields. *Proc. Natl Acad. Sci. USA* **112**, 7668–7672 (2015).
4. Ménez, B. et al. Abiotic synthesis of amino acids in the recesses of the oceanic lithosphere. *Nature* **564**, 59–63 (2018).
5. Klein, F. & Bach, W. Fe-Ni-Co-O-S phase relations in peridotite–seawater interactions. *J. Petrol.* **50**, 37–59 (2009).
6. Martin, W. F. & Russell, M. J. On the origin of biochemistry at an alkaline hydrothermal vent. *Philos. Trans. R. Soc. B* **362**, 1887–1925 (2007).
7. Preiner, M. et al. Serpentinization: connecting geochemistry, ancient metabolism and industrial hydrogenation. *Life* **8**, 41 (2018).
8. Sleep, N. H., Bird, D. K. & Pope, E. C. Serpentinite and the dawn of life. *Philos. Trans. R. Soc. B* **366**, 2857–2869 (2011).
9. Schrenk, M. O., Brazelton, W. J. & Lang, S. Q. Serpentinization, carbon, and deep life. *Rev. Miner. Geochem.* **75**, 575–606 (2013).
10. Arndt, N. T. & Nisbet, E. G. Processes on the young Earth and the habitats of early life. *Annu. Rev. Earth Planet. Sci.* **40**, 521–549 (2012).
11. Fuchs, G. Alternative pathways of carbon dioxide fixation: insights into the early evolution of life? *Annu. Rev. Microbiol.* **65**, 631–658 (2011).
12. Müller, V., Chowdhury, N. P. & Basen, M. Electron bifurcation: a long-hidden energy-coupling mechanism. *Annu. Rev. Microbiol.* **72**, 331–353 (2018).
13. Ragsdale, S. W. & Pierce, E. Acetogenesis and the Wood–Ljungdahl pathway of $CO_2$ fixation. *Biochim. Biophys. Acta* **1784**, 1873–1898 (2008).
14. Sousa, F. L. & Martin, W. F. Biochemical fossils of the ancient transition from geoenergetics to bioenergetics in prokaryotic one carbon compound metabolism. *Biochim. Biophys. Acta* **1837**, 964–981 (2014).
15. Weiss, M. C. et al. The physiology and habitat of the last universal common ancestor. *Nat. Microbiol.* **1**, 16116 (2016).
16. Huber, C. & Wächtershäuser, G. Activated acetic acid by carbon fixation on (Fe,Ni)S under primordial conditions. *Science* **276**, 245–248 (1997).
17. He, C., Tian, G., Liu, Z. & Feng, S. A mild hydrothermal route to fix carbon dioxide to simple carboxylic acids. *Org. Lett.* **12**, 649–651 (2010).
18. Varma, S. J., Muchowska, K. B., Chatelain, P. & Moran, J. Native iron reduces $CO_2$ to intermediates and endproducts of the acetyl-CoA pathway. *Nat. Ecol. Evol.* **2**, 1019–1024 (2018).
19. Roldan, A. et al. Bio-inspired $CO_2$ conversion by iron sulfide catalysts under sustainable conditions. *Chem. Commun.* **51**, 7501–7504 (2015).
20. Rajendran, S. & Nasir, S. Hydrothermal altered serpentinized zone and a study of Ni-magnesioferrite–magnetite–awaruite occurrences in Wadi Hibi, Northern Oman Mountain: discrimination through ASTER mapping. *Ore Geol. Rev.* **62**, 211–226 (2014).
21. Russell, M. J. & Hall, A. J. The emergence of life from iron monosulphide bubbles at a submarine hydrothermal redox and pH front. *J. Geol. Soc. London* **154**, 377–402 (1997).
22. Rickard, D. & Luther, G. W. Chemistry of iron sulfides. *Chem. Rev.* **107**, 514–562 (2007).
23. McCollom, T. M. & Seewald, J. S. Serpentinites, hydrogen, and life. *Elements* **9**, 129–134 (2013).
24. Hunger, S. & Benning, L. G. Greigite: a true intermediate on the polysulfide pathway to pyrite. *Geochem. Trans.* **8**, 1 (2007).
25. Findlay, A. J. et al. Iron and sulfide nanoparticle formation and transport in nascent hydrothermal vent plumes. *Nat. Commun.* **10**, 1597 (2019).
26. Schmitt-Kopplin, P. et al. High molecular diversity of extraterrestrial organic matter in Murchison meteorite revealed 40 years after its fall. *Proc. Natl Acad. Sci. USA* **107**, 2763–2768 (2010).
27. Dayhoff, M. O. & Eck, R. V. Evolution of the structure of ferredoxin based on surviving relics of primitive amino acid sequences. *Science* **152**, 363–366 (1966).
28. White, L. M., Bhartia, R., Stucky, G. D., Kanik, I. & Russell, M. J. Mackinawite and greigite in ancient alkaline hydrothermal chimneys: identifying potential key catalysts for emergent life. *Earth Planet. Sci. Lett.* **430**, 105–114 (2015).
29. Kelley, D. S. et al. An off-axis hydrothermal vent field near the Mid-Atlantic Ridge at 30° N. *Nature* **412**, 145–149 (2001).
30. Kelley, D. S., Baross, J. A. & Delaney, J. R. Volcanoes, fluids, and life at mid-ocean ridge spreading centers. *Annu. Rev. Earth Planet. Sci.* **30**, 385–491 (2002).
31. Lang, S. Q., Butterfield, D. A., Schulte, M., Kelley, D. S. & Lilley, M. D. Elevated concentrations of formate, acetate and dissolved organic carbon found at the Lost City hydrothermal field. *Geochim. Cosmochim. Acta* **74**, 941–952 (2010).
32. Lang, S. Q. et al. Deeply-sourced formate fuels sulfate reducers but not methanogens at Lost City hydrothermal field. *Sci. Rep.* **8**, 755 (2018).
33. Etiope, G. & Sherwood Lollar, B. Abiotic methane on Earth. *Rev. Geophys.* **51**, 276–299 (2013).
34. Horita, J. & Berndt, M. E. Abiogenic methane formation and isotopic fractionation under hydrothermal conditions. *Sci. Rep.* **285**, 1055–1057 (1999).
35. Schuchmann, K. & Müller, V. Direct and reversible hydrogenation of $CO_2$ to formate by a bacterial carbon dioxide reductase. *Science* **342**, 1382–1385 (2013).
36. Eickenbusch, P. et al. Origin of short-chain organic acids in serpentinite mud volcanoes of the Mariana convergent margin. *Front. Microbiol.* **10**, 1729 (2019).
37. Etiope, G. & Schoell, M. Abiotic gas: atypical, but not rare. *Elements.* **10**, 291–296 (2014).
38. McCollom, T. M. & Seewald, J. S. Experimental constraints on the hydrothermal reactivity of organic acids and acid anions: I. Formic acid and formate. *Geochim. Cosmochim. Acta* **67**, 3625–3644 (2003).
39. McCollom, T. M. & Seewald, J. S. Carbon isotope composition of organic compounds produced by abiotic synthesis under hydrothermal conditions. *Earth Planet. Sci. Lett.* **243**, 74–84 (2006).
40. McCollom, T. M. & Seewald, J. S. A reassessment of the potential for reduction of dissolved $CO_2$ to hydrocarbons during serpentinization of olivine. *Geochim. Cosmochim. Acta* **65**, 3769–3778 (2001).
41. Menon, S. & Ragsdale, S. W. Unleashing hydrogenase activity in carbon monoxide dehydrogenase/acetyl-CoA synthase and pyruvate:ferredoxin oxidoreductase. *Biochemistry* **35**, 15814–15821 (1996).
42. Jeoung, J.-H. & Dobbek, H. Carbon dioxide activation at the Ni,Fe-cluster of anaerobic carbon monoxide dehydrogenase. *Conserv. Exhib.* **318**, 1461–1464 (2007).
43. Dobbek, H., Svetlitchnyi, V., Gremer, L., Huber, R. & Meyer, O. Crystal structure of a carbon monoxide dehydrogenase reveals a [Ni-4Fe-5S] cluster. *Science* **293**, 1281–1285 (2001).
44. Chabrière, E. et al. Crystal structures of the key anaerobic enzyme pyruvate ferredoxin oxidoreductase free and in complex with pyruvate. *Nat. Struct. Biol.* **6**, 182–190 (1999).
45. Volbeda, A. et al. Crystal structure of the nickel-iron hydrogenase from *Desulfovibrio gigas*. *Nature* **373**, 580–587 (1995).
46. Martin, W. F. Carbon-metal bonds: rare and primordial in metabolism. *Trends Biochem. Sci.* **44**, 807–818 (2019).
47. Buckel, W. & Thauer, R. K. Flavin-based electron bifurcation, ferredoxin, flavodoxin, and anaerobic respiration with protons (Ech) or NAD+(Rnf) as electron acceptors: a historical review. *Front. Microbiol.* **9**, 401 (2018).
48. Vasiliadou, R., Dimov, N., Szita, N., Jordan, S. & Lane, N. Possible mechanisms of $CO_2$ reduction by $H_2$ via prebiotic vectorial electrochemistry. *Interface Focus* **9**, 20190073 (2018).
49. Kaufmann, M. On the free energy that drove primordial anabolism. *Int. J. Mol. Sci.* **10**, 1853–1871 (2009).
50. Patel, B. H., Percivalle, C., Ritson, D. J., Duffy, C. D. & Sutherland, J. D. Common origins of RNA, protein and lipid precursors in a cyanosulfidic protometabolism. *Nat. Chem.* **7**, 301–307 (2015).
51. Lane, N. & Martin, W. F. The origin of membrane bioenergetics. *Cell* **151**, 1406–1416 (2012).
52. Jordan, S. F., Nee, E. & Lane, N. Isoprenoids enhance the stability of fatty acid membranes at the emergence of life potentially leading to an early lipid divide. *Interface Focus* **9**, 20100067 (2019).
53. Jordan, S. F. et al. Promotion of protocell self-assembly from mixed amphiphiles at the origin of life. *Nat. Ecol. Evol.* **3**, 1705–1714 (2019).
54. Kitadai, N. et al. Metals likely promoted protometabolism in early ocean alkaline hydrothermal systems. *Sci. Adv.* **5**, eaav7848 (2019).
55. Muchowska, K. B. et al. Metals promote sequences of the reverse Krebs cycle. *Nat. Ecol. Evol.* **1**, 1716–1721 (2017).
56. Lovley, D. R. & Phillips, E. J. Organic matter mineralization with reduction of ferric iron in anaerobic sediments. *Appl. Environ. Microbiol.* **51**, 683–689 (1986).

57. Igarashi, K., Yamamura, Y. & Kuwabara, T. Natural synthesis of bioactive greigite by solid–gas reactions. *Geochim. Cosmochim. Acta* **191**, 47–57 (2016).
58. Kato, S., Yumoto, I. & Kamagata, Y. Isolation of acetogenic bacteria that induce biocorrosion by utilizing metallic iron as the sole electron donor. *Appl. Environ. Microbiol.* **81**, 67–73 (2015).
59. Mayumi, D. et al. Carbon dioxide concentration dictates alternative methanogenic pathways in oil reservoirs. *Nat. Commun.* **4**, 1998 (2013).
60. Deng, X., Chan, C. K. & Tüysüz, H. Spent tea leaf templating of cobalt-based mixed oxide nanocrystals for water oxidation. *ACS Appl. Mater. Interfaces* **8**, 32488–32495 (2016).
61. Yu, M., Moon, G., Bill, E. & Tüysüz, H. Optimizing Ni−Fe oxide electrocatalysts for oxygen evolution reaction by using hard templating as a toolbox. *ACS Appl. Energy Mater.* **2**, 1199–1209 (2019).
62. Hanselmann, K. W. Microbial energetics applied to waste repositories. *Experientia* **47**, 645–687 (1991).
63. Amend, J. P. & Shock, E. L. Energetics of overall metabolic reactions of thermophilic and hyperthermophilic archaea and bacteria. *FEMS Microbiol. Rev.* **25**, 175–243 (2001).
64. Wang, G., Spivack, A. J. & Hondt, S. D. Gibbs energies of reaction and microbial mutualism in anaerobic deep subseafloor sediments of ODP Site 1226. *Geochim. Cosmochim. Acta* **74**, 3938–3947 (2010).
65. Wagner, T., Ermler, U. & Shima, S. The methanogenic $CO_2$ reducing-and-fixing enzyme is bifunctional and contains 46 [4Fe-4S] clusters. *Science* **354**, 114–117 (2015).
66. Mayumi, D. et al. Methane production from coal by a single methanogen. *Science* **354**, 222–225 (2016).
67. Hoffman, B. M. et al. Mechanism of nitrogen fixation by nitrogenase: the next stage. *Chem. Rev.* **114**, 4041–4062 (2014).


## Acknowledgements

We thank Y. Dai for setting up gas analysis for the awaruite experiments, A. do Nascimento Vieira for performing parts of the revision experiments, A. Bähr and P. Lim for scientific support and J. C. Xavier for discussions. For funding, J.M., W.F.M. and H.T. thank the VW foundation (no. 96_742). W.F.M. and H.T. thank Deutsche Forschungsgemeinschaft (no. MA-1426/21-1/TU 315/8-1) and W.F.M. thanks the European Research Council (no. ERC 666053). This work is partly supported by IMPRS-RECHARGE and MAXNET Energy consortium of the Max Planck Society. K.I. and Y.K. thank JSPS KAKENHI Grant-in-Aid for Scientific Research on Innovative Areas (K.I., no. JP17H05240; Y.K., no. 26106004). K.I. is also supported by Grant-in-Aid for Young Scientists B (no. JP17K15255). J.M. thanks the European Research Council (no. ERC 639170) and ANR LabEX (no. ANR-10-LABX-0026 CSC). This work was also partly supported by Nanotechnology Platform Program (Molecule and Material Synthesis) of the Ministry of Education, Culture, Sports, Science and Technology, Japan.

## Author contributions

W.F.M. wrote the initial draft of the main text and all authors edited the manuscript. W.F.M., H.T., J.M. and M.P. designed the awaruite experiments. M.P. performed the awaruite experiments and assembled the results for the main text and Supplementary Information material. K.B.M. designed and performed the magnetite experiments. S.J.V. performed exploratory experiments with magnetite. Design of the greigite experiments was done by K.I. and Y.K. K.I. performed the experiments. H.T. and M.Y. designed and synthesized the awaruite nanoparticles and performed XRD and transmission electron microscopy measurements for the magnetite and awaruite experiments. M.K.N. performed and interpreted the thermodynamics calculations. K.K., J.M., H.T. and M.P. formulated the $H_2$ reduction mechanism shown in the Supplementary Information.

## Competing interests

The authors declare no competing interests.

## Additional information

**Extended data** is available for this paper at https://doi.org/10.1038/s41559-020-1125-6.

**Supplementary information** is available for this paper at https://doi.org/10.1038/s41559-020-1125-6.

**Correspondence and requests for materials** should be addressed to H.T., J.M. or W.F.M.

**Reprints and permissions information** is available at www.nature.com/reprints.

**Publisher's note** Springer Nature remains neutral with regard to jurisdictional claims in published maps and institutional affiliations.

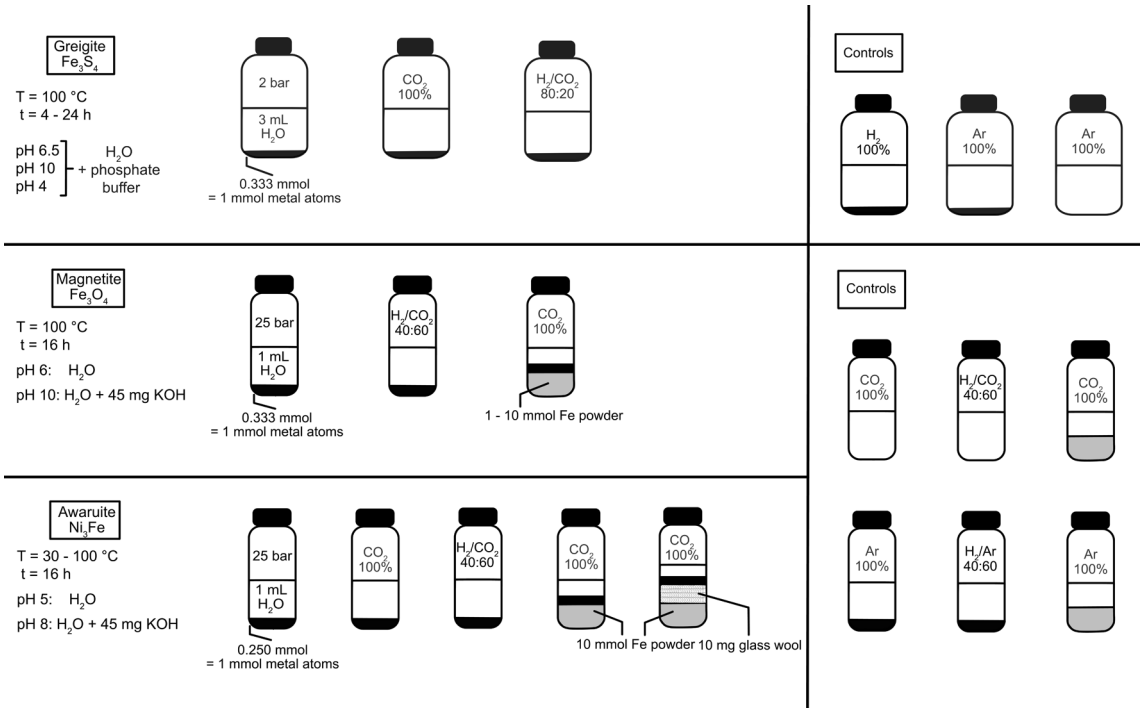


**Extended Data Fig. 1 | Overview of the main experiments performed in this study.** Three different iron-containing hydrothermal minerals were tested for their ability to catalyse the reaction between $CO_2$ and $H_2$: greigite ($Fe_3S_4$), magnetite ($Fe_3O_4$), and awaruite ($Ni_3Fe$).

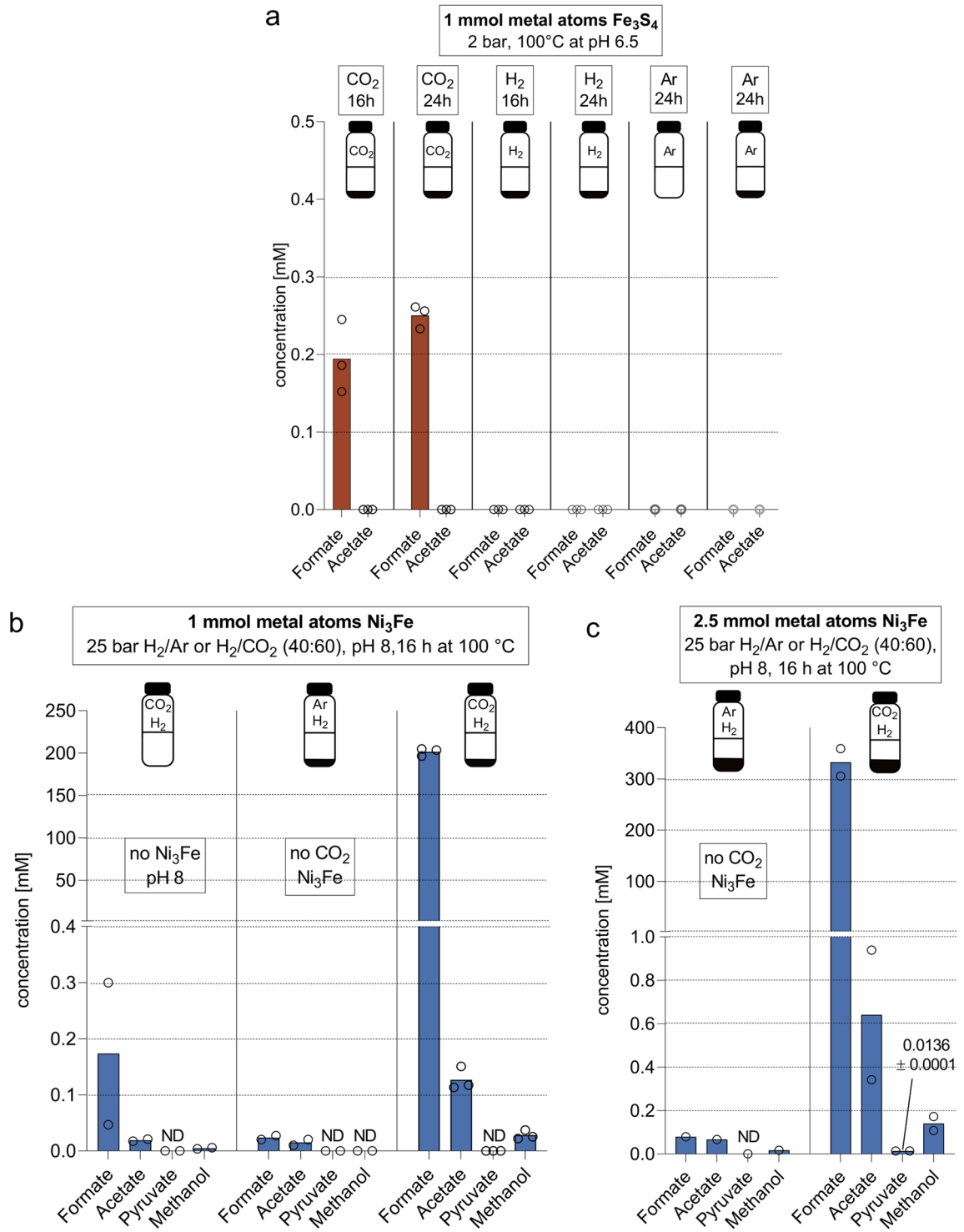


**Extended Data Fig. 2 | Background controls for $CO_2$ fixation. a** Control runs for greigite experiments—each run was performed either in the absence of $H_2$ or $CO_2$, or both. Circles show individual measurements. $CO_2$-only and $H_2$-only controls were performed at least in triplicate – values of 0 are not shown by the logarithmic scale. Four types of control experiments under the conditions of greigite experiments were performed with the catalyst: one under 100% $CO_2$ atmosphere, one under 100% $H_2$ atmosphere and two under Ar atmosphere (one with, one without catalyst). The mass spectra of the argon-controls are listed in the supplemental material. The $CO_2$-only experiments show that formate can be formed in small amounts without $H_2$ gas, suggesting that the electrons necessary for $CO_2$ reduction can also come from greigite's $Fe^{2+}$ ions, either by forming $H_2$ from water or by a direct reduction of $CO_2$. The latter seems less probable as the step from $CO_2$ to formate is a 2-electron reaction, which electrons $Fe^{2+}$ cannot provide (see also the proposed mechanism in Extended Data Fig. 10). **b** Comparison between background and product concentration in awaruite experiments with 1 mmol metal atoms $Ni_3Fe$ (16 h at 100 °C, 25 bar, pH > 7). Both $CO_2$ fixation background without $Ni_3Fe$ and the background of $Ni_3Fe$ itself under an $Ar/H_2$ atmosphere are significantly lower than after $H_2$-dependent $CO_2$ reduction with $Ni_3Fe$. **c** Comparing background and product concentration in awaruite experiments with 2.5 mmol metal atoms $Ni_3Fe$ (16 h at 100 °C, 25 bar, pH > 7). More details on the background contamination in awaruite and magnetite experiments are listed in Supplementary Tables 3–6.

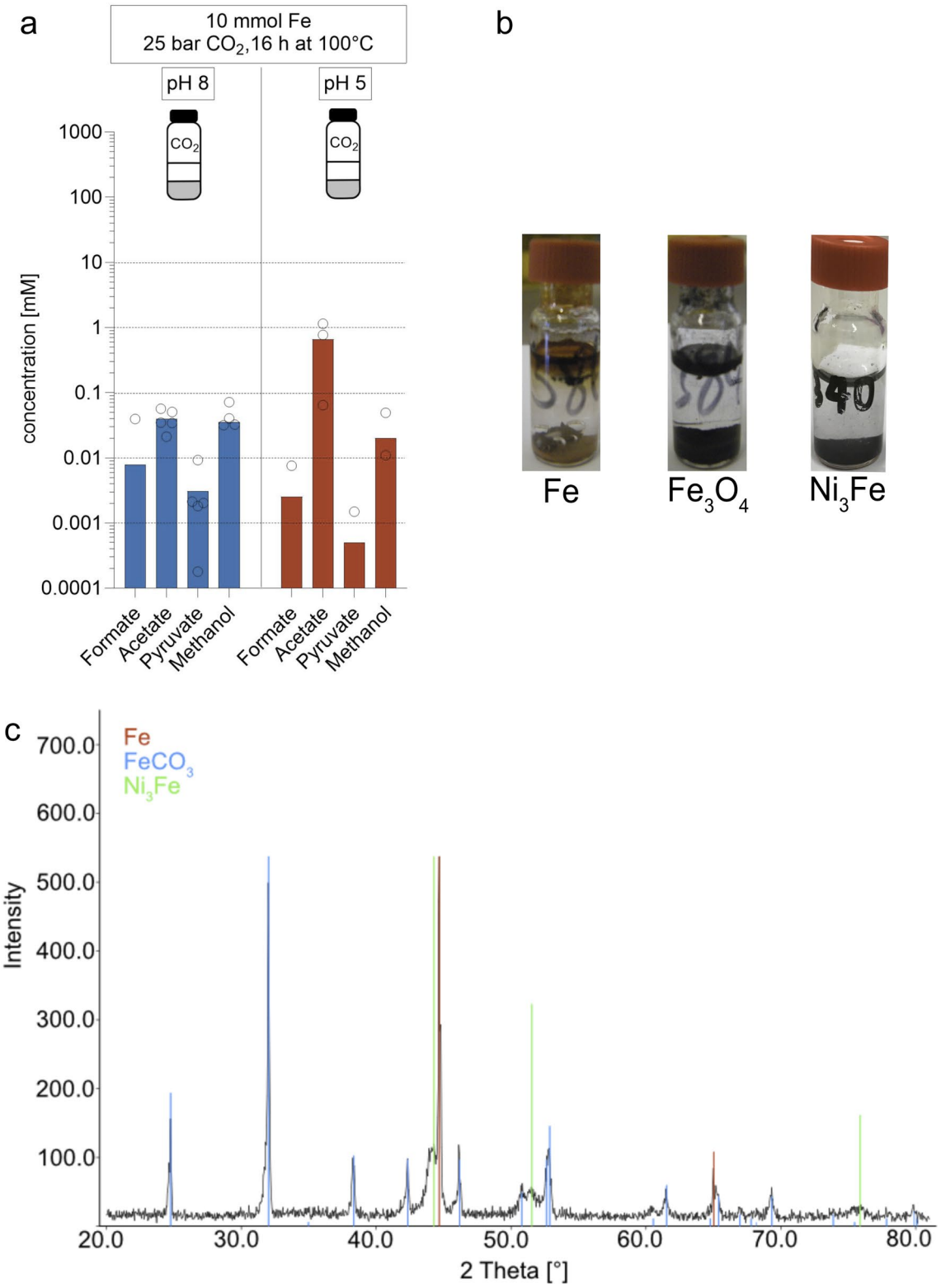


**Extended Data Fig. 3 | Controls with added $Fe^0$ powder. a** Control for internal $Fe^0$ runs (relevant to magnetite and awaruite experiments). Red: pH < 7; Blue: pH > 7. Circles show individual measurements, all controls were performed in at least triplicate – values of 0 are not shown by the logarithmic scale. As shown in Varma et al.[18], a KOH workup after the reaction was necessary prior to analysis. Here we show that KOH can also be added before the reaction (blue bars) in order to liberate the products into the solution. For reactions at lower pH (red bars), KOH was added afterwards. In both cases Fe powder promotes the reduction of $CO_2$ to formate, acetate, pyruvate and methanol. The exact mechanism remains unclear, but it is probable that the Fe powder is being oxidized, leading to the production of $H_2$ from $H_2O$. **b** Pictures after the reaction at pH 8, 16 h, 100 °C, 25 bar $CO_2/H_2$, showing the visual level of oxidation of $Fe^0$, $Fe_3O_4$ and $Ni_3Fe$. **c** XRD of iron powder after a reaction with 0.125 mmol $Ni_3Fe$ on top (25 bar $CO_2$, 16 h, pH 8, 100 °C), the results of the $CO_2$ fixation are shown in Extended Data Fig. 6. The XRD spectrum shows that a major part of the iron surface is converted into iron(II) carbonate (siderite, $FeCO_3$), thus confirming the oxidation of the iron powder and the precipitation of $Fe^{2+}$ ions with carbonate at the same time.

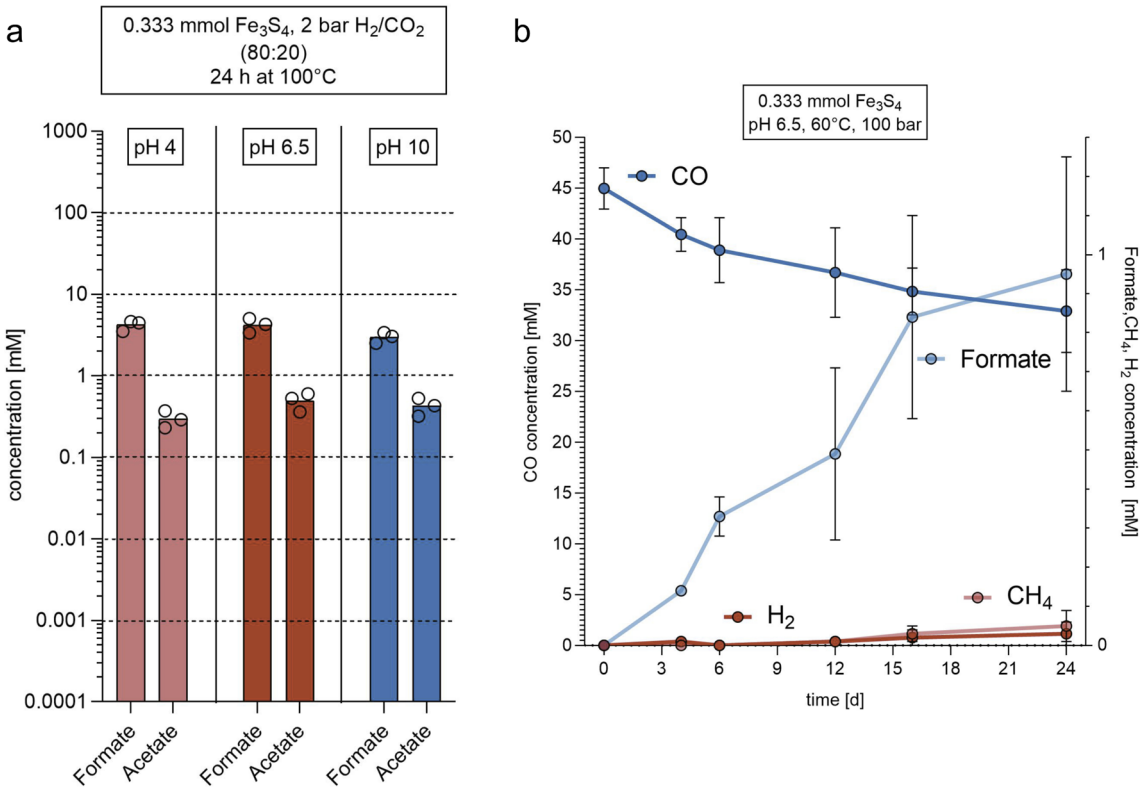


**Extended Data Fig. 4 | Influence of pH and high-pressure CO experiments for greigite. a** Influence of pH on greigite reactions. Red: pH < 7; Blue: pH > 7. Circles show individual measurements, all measurements performed in at least triplicate. The distribution of carbon fixation products in greigite reactions remains stable with changing pH. **b** Time course experiment of high-pressure methane and formate production from CO under greigite catalysis (liquid phase, 150 mL) at 60 °C and 100 bar. Using CO gas instead of $CO_2$ and $H_2$ does not explain the amount of methane produced (up to 0.04 mM). The rationale for using CO as a sole reactant stems from previous reports where small organics were obtained in appreciable quantities[16]. In reactions of CO with greigite and water, no organic products were found other than formate, whose carbon has the same redox state as CO.

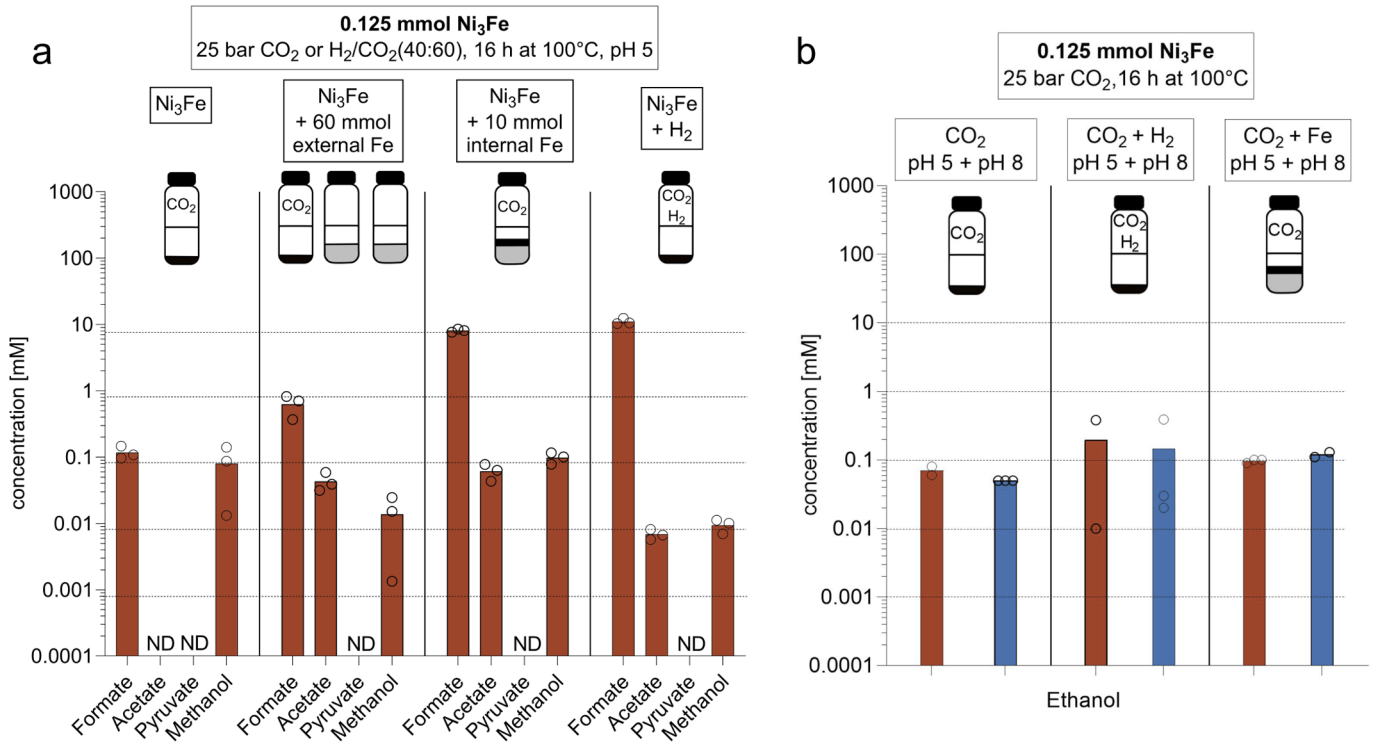


**Extended Data Fig. 5 | $Fe^0$ as external and internal $H_2$ source and ethanol occurrence in awaruite experiments. a** Screen of the quantity of $Fe^0$ as $H_2$ source. As a native metal compound, awaruite could serve as an electron donor and/or a catalyst. To establish the catalytic activity of the nanoparticular awaruite and the ability of $Fe^0$ powder to serve as an $H_2$ delivery system, the concentration of hydrogen gas within the reactor runs was gradually increased. First, 6 neighbouring vials filled with 10 mmol (560 mg) of iron powder ('external iron') each provided a small amount of $H_2$ to the atmosphere inside the pressure reactor. By adding 10 mmol iron powder into reaction vials ("internal iron") and placing the nanoparticular awaruite on top of it, especially formate concentration was pushed towards very high yields (8 mM at pH 5; 100 mM at pH 8, depicted in main Fig. 3b). **b** Occurrence of ethanol in $Ni_3Fe$ reactions. Red: pH < 7; Blue: pH > 7. Circles show individual measurements; all measurements were performed in at least duplicate – values of 0 are not shown by the logarithmic scale. Ethanol was detected in concentrations up to over 0.1 mM. Its concentration fluctuated over the course of experiments, leading to the conclusion that it might be a product of decarboxylation of pyruvate or other side reactions.

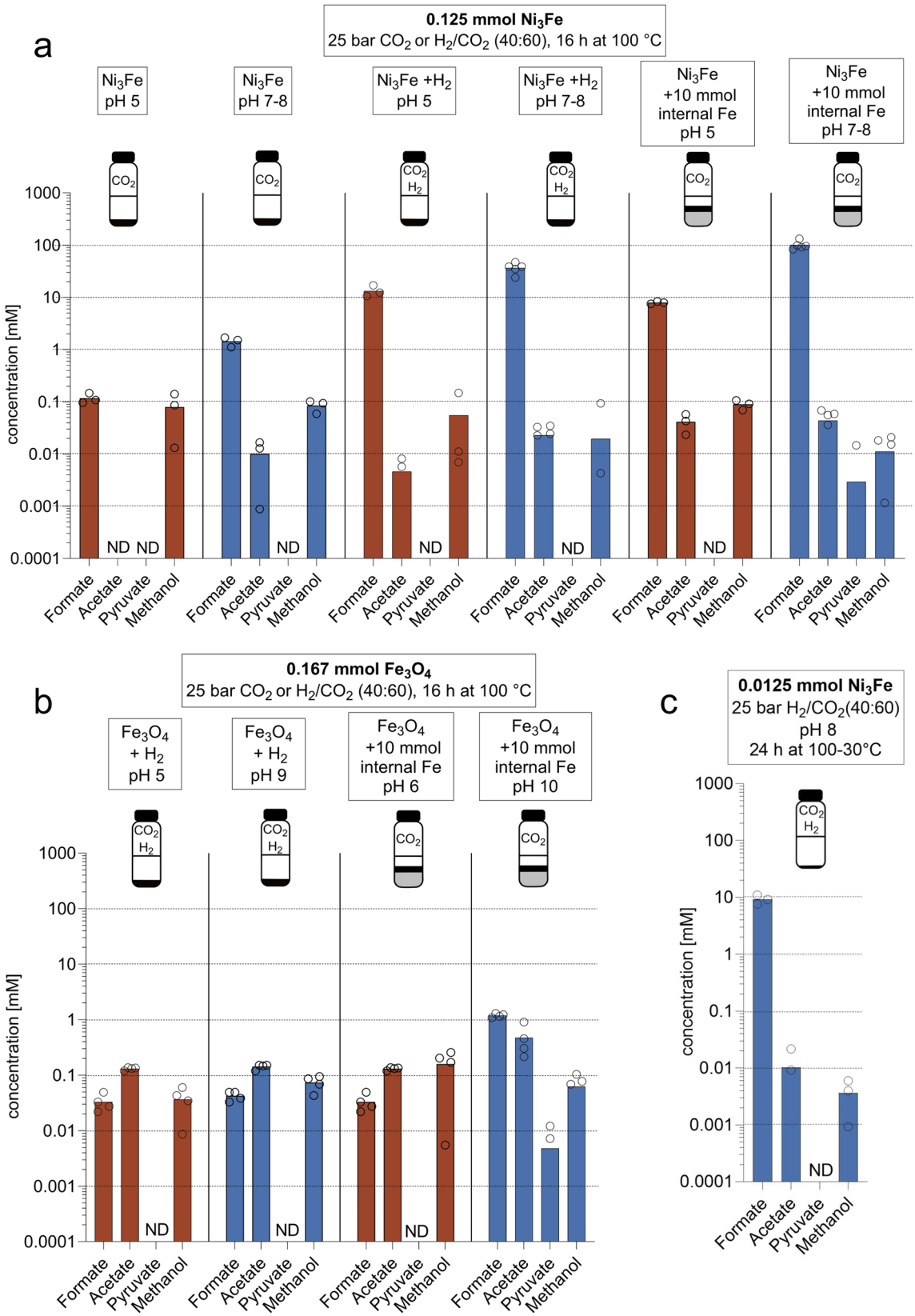


**Extended Data Fig. 6 | Lower amounts of catalyst in magnetite and awaruite experiments. a** $Ni_3Fe$ catalysis of $CO_2$ fixation with 0.125 mmol catalyst (0.5 mmol metal atoms). Reactions mixtures with pH < 7 were not treated with KOH after the reaction. **b** $Fe_3O_4$ catalysis of $CO_2$ fixation with 0.167 mmol catalyst (0.5 mmol metal atoms). Reactions mixtures with pH < 7 were treated with KOH after reaction. Using less magnetite and less awaruite still yields a noticeable amount of product. **c** $Ni_3Fe$ catalysis of $CO_2$ fixation at 100–30 °C. Red: pH < 7; Blue: pH > 7.Circles show individual measurements, all measurements were performed in at least triplicate – values of 0 are not shown by the logarithmic scale. Under this thermal gradient (8 h at 100 °C, 8 h at 70 °C, 8 h at 30 °C), even very small amounts (12.5 μmol = 50 μmol of metal atoms) of $Ni_3Fe$ suffice to produce notable amounts of formate, acetate and methanol.

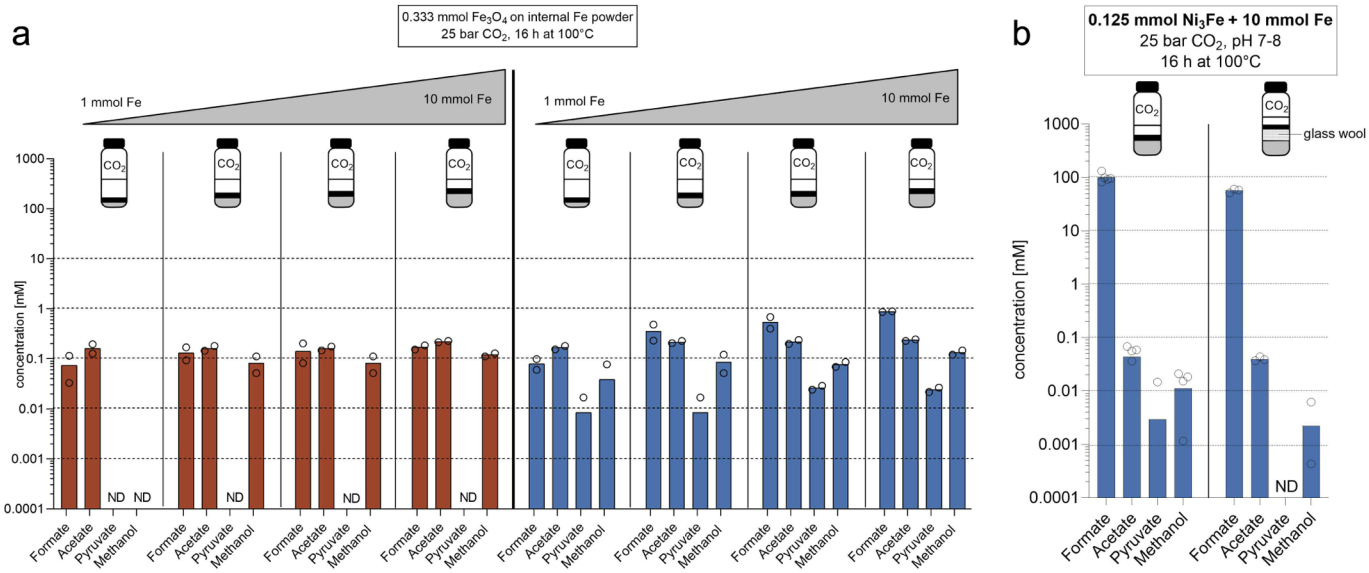


**Extended Data Fig. 7 | Effect of physical contact between $Fe^0$ as internal $H_2$ source and catalyst and effect of $Fe^0$ amount. a** Effect of $Fe^0$ as internal $H_2$ source with magnetite as catalyst. Red: pH < 7; Blue: pH > 7. Circles show individual measurements, all measurements were performed in duplicate – values of 0 are not shown by the logarithmic scale. In the absence of $H_2$ and with $Fe^0$ as reductant, $CO_2$ can be reduced in water in the presence of $Fe_3O_4$. Pyruvate accumulates at detectable levels at pH 10 but not at pH 6. The product increase with increasing iron quickly reaches an unexpected maximum, considering the minor differences in product concentration between the two samples with the highest Fe amount. A likely reason is that not the entire bulk of the iron powder reacts/becomes oxidized, but only the surface, thus inhibiting further interaction of the water molecules with the unreacted iron underneath the iron oxide and/or iron carbonate layer formed. **b** Separating awaruite (0.125 mmol $Ni_3Fe$ = 0.5 mmol metal atoms) and internal iron powder. Circles show individual measurements, all measurements in triplicate – values of 0 are not shown by the logarithmic scale. Physical contact between the mineral and native iron is not required for product formation. As shown in Extended Data Fig. 3, placing the catalysts directly on the iron powder in order to "harvest" the nascent hydrogen ascending from the iron powder has the disadvantage that products on the surface of the iron will mix with the ones from awaruite (or magnetite). By tightly packing ca. 10 mg of decontaminated glass wool between iron and awaruite, this effect can be decreased. Although in the initial experiments, no pyruvate could be detected, the other products were formed in appreciable amounts.

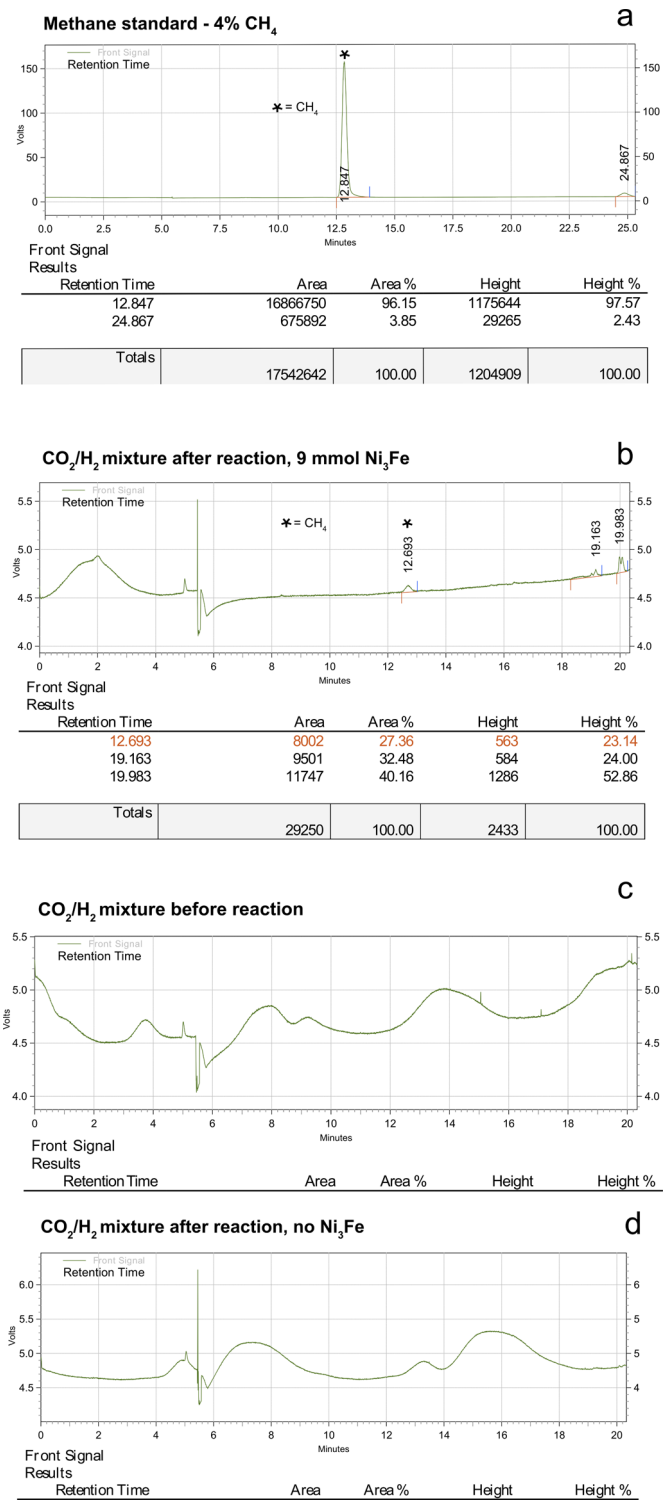


**Extended Data Fig. 8 | Detection of methane by GC-FID for awaruite experiments. a** Gas analysis of 4% (40,000 ppm) methane standard**. b** $CO_2/H_2$ reaction with $Ni_3Fe$ (awaruite) as catalyst. These measurements show that $CH_4$ is formed, although only in very small amounts. According to the methane standard measurement, the methane outcome of a typical experiment (16 h, 100 °C, 60:40 $CO_2/H_2$ atmosphere, 25 bar) containing 9 mmol of awaruite within one reactor run is roughly 19 ppm (determined by a one-point calibration). Two controls were performed: **c** one with the reactor pressurized (25 bar) with the 60:40 $CO_2/H_2$ gas mixture, and **d** one after subjecting the $CO_2/H_2$ gas mixture to the typical experimental conditions (16 h, 100 °C) within the otherwise empty reactor. Neither control experiment showed traces of methane.

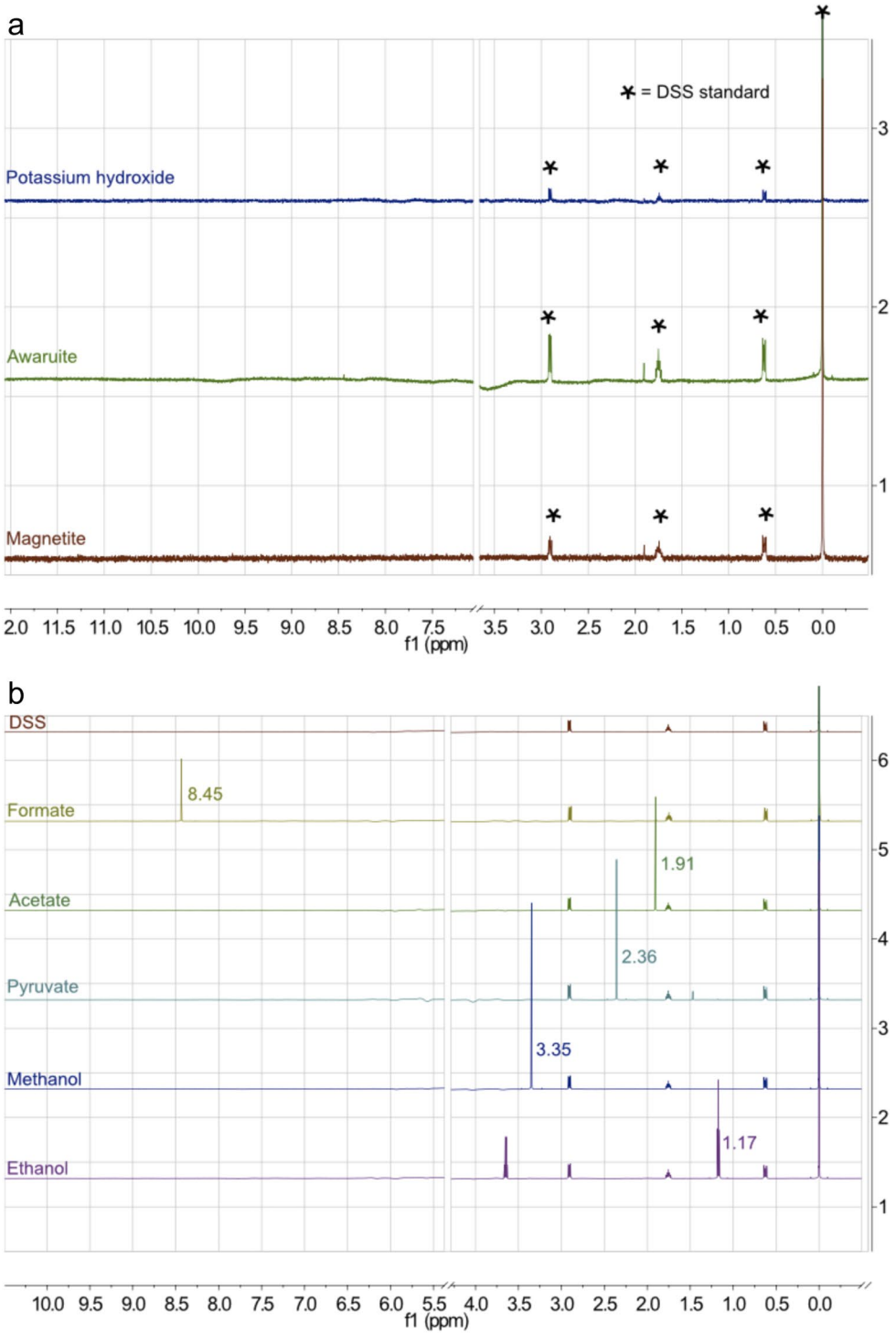


**Extended Data Fig. 9 | $^1$H-NMR controls for catalysts and reagents and shifts of product peaks in the magnetite and awaruite experiments. a** $^1$H-NMR material controls for catalysts and reagents used for experiments with NMR product detection. Awaruite and magnetite were tested for surface contamination by treating it with a potassium hydroxide solution to cleave potential contaminants from the surface. Also potassium hydroxide was tested for contaminations. **b** $^1$H NMR chemical shifts of product peaks observed and quantified in the magnetite and awaruite experiments. Quantification was achieved using two-point linear regression analysis.

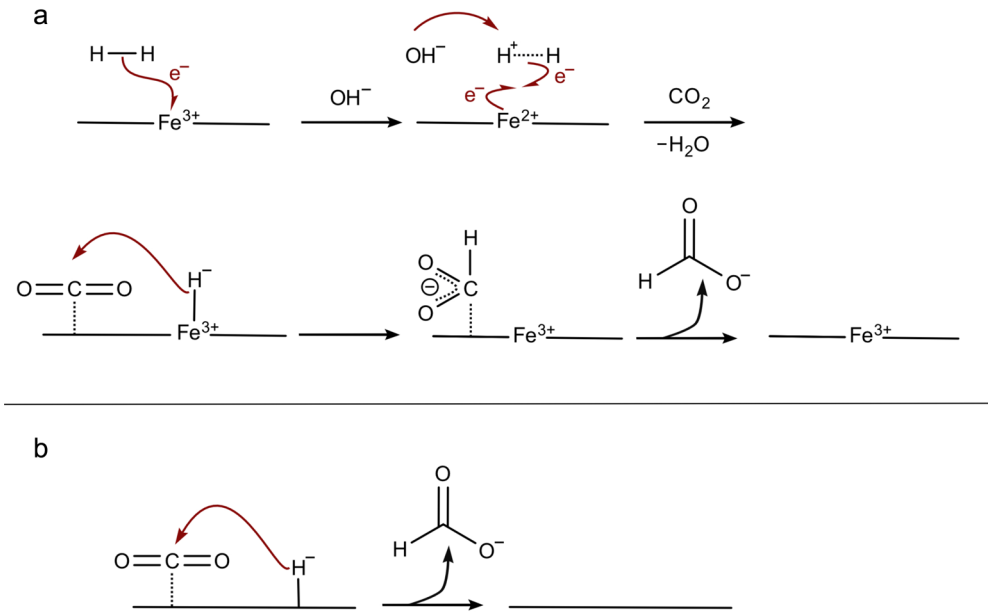


**Extended Data Fig. 10 | Proposed mechanisms for $CO_2$ reduction with $H_2$ catalysed by hydrothermal minerals.** We propose an ionic mechanism for the catalysed two-electron reduction of $CO_2$ to formate in water for all three minerals **a** Proposed mechanism for $CO_2$ reduction with $H_2$ catalysed by $Fe_3O_4$ (or $Fe_3S_4$). An $H_2$ molecule approaches the $Fe_3O_4$ (or $Fe_3S_4$) surface and reduces $Fe^{3+}$ to $Fe^{2+}$. The generated $H_2^+$ is unstable and decomposes to $H^+$, assisted by $OH^-$ (accounting for increased product formation at pH > 7 in magnetite experiments) – and to a hydrogen atom (H·) which picks up an electron from $Fe^{2+}$ to become a hydride ($H^-$). Hydride mechanisms were described in previous literature[67]. $CO_2$ on the other hand physisorbs on the magnetite surface and reacts with the hydride to yield $HCOO^-$ which is displaced from the surface by $OH^-$. Observations from experiments not discussed in this publication show, that experiments with minerals only containing ferrous iron (FeO and FeS) give far lower yields of $CO_2$ fixation products. **b** Proposed mechanism of $CO_2$ reduction catalysed by $Ni_3Fe$. As $Ni_3Fe$ only consists of zero-valent metals, $H_2$ can dissociate on the metal surface. Then, the H atoms diffuse into awaruite where they can capture mobile ("free") electrons from the conduction band of the metal alloy.

Corresponding author(s): William F. Martin (bill@hhu.de)
Joseph Moran (moran@unistra.fr)
Harun Tüysüz (tueysuez@mpi-muelheim.mpg.de)

Last updated by author(s): Jan 13, 2020

# Reporting Summary

Nature Research wishes to improve the reproducibility of the work that we publish. This form provides structure for consistency and transparency in reporting. For further information on Nature Research policies, see Authors & Referees and the Editorial Policy Checklist.

## Statistics

For all statistical analyses, confirm that the following items are present in the figure legend, table legend, main text, or Methods section.

| n/a | Confirmed | |
|---|---|---|
| ☐ | ☒ | The exact sample size (*n*) for each experimental group/condition, given as a discrete number and unit of measurement |
| ☐ | ☒ | A statement on whether measurements were taken from distinct samples or whether the same sample was measured repeatedly |
| ☒ | ☐ | The statistical test(s) used AND whether they are one- or two-sided<br>*Only common tests should be described solely by name; describe more complex techniques in the Methods section.* |
| ☒ | ☐ | A description of all covariates tested |
| ☒ | ☐ | A description of any assumptions or corrections, such as tests of normality and adjustment for multiple comparisons |
| ☒ | ☐ | A full description of the statistical parameters including central tendency (e.g. means) or other basic estimates (e.g. regression coefficient) AND variation (e.g. standard deviation) or associated estimates of uncertainty (e.g. confidence intervals) |
| ☒ | ☐ | For null hypothesis testing, the test statistic (e.g. *F*, *t*, *r*) with confidence intervals, effect sizes, degrees of freedom and *P* value noted<br>*Give P values as exact values whenever suitable.* |
| ☒ | ☐ | For Bayesian analysis, information on the choice of priors and Markov chain Monte Carlo settings |
| ☒ | ☐ | For hierarchical and complex designs, identification of the appropriate level for tests and full reporting of outcomes |
| ☒ | ☐ | Estimates of effect sizes (e.g. Cohen's *d*, Pearson's *r*), indicating how they were calculated |

*Our web collection on statistics for biologists contains articles on many of the points above.*

## Software and code

Policy information about availability of computer code

| | |
|---|---|
| Data collection | For HPLC data collection (greigite experiments), Chromatography Data Station (version 2.0, Hitachi) software was used.<br>For HPLC-MS data collection, Compass Hystar (version 3.2, Bruker) software was used.<br>For GC-FID/TCD data collection, GCMS Solution (version 2.32, Shimadzu) software was used.<br>For GC-MS data collection, GCMS Solution (version 4.50, Shimadzu) software was used.<br>For HPLC data collection (awaruite experiments), Chromeleon (7.2) software was used. |
| Data analysis | For HPLC data analysis (greigite experiments), Chromatography Data Station (version 2.0, Hitachi) software was used.<br>For HPLC-MS data analysis, Data Analysis (version 4.0.2, Bruker) software was used.<br>For GC-FID/TCD data analysis, GCMS Solution (version 2.32, Shimadzu) software was used.<br>For GC-MS data analysis, GCMS Solution (version 4.50, Shimadzu) software was used.<br>For NMR data analysis, Mestrenova (10.0.2) software was used (magnetite and awaruite experiments). Excel and Prism were used for data analysis of experimental results (all experiments). |

For manuscripts utilizing custom algorithms or software that are central to the research but not yet described in published literature, software must be made available to editors/reviewers. We strongly encourage code deposition in a community repository (e.g. GitHub). See the Nature Research guidelines for submitting code & software for further information.

## Data

Policy information about availability of data

All manuscripts must include a data availability statement. This statement should provide the following information, where applicable:

- Accession codes, unique identifiers, or web links for publicly available datasets
- A list of figures that have associated raw data
- A description of any restrictions on data availability

We provide the data (including SD) of our main Figure 2 in the supplementary information (Table S1) and all data of the thermodynamic calculations in an additional excel table (Table S2).

# Field-specific reporting

Please select the one below that is the best fit for your research. If you are not sure, read the appropriate sections before making your selection.

☐ Life sciences ☐ Behavioural & social sciences ☒ Ecological, evolutionary & environmental sciences

For a reference copy of the document with all sections, see nature.com/documents/nr-reporting-summary-flat.pdf

# Ecological, evolutionary & environmental sciences study design

All studies must disclose on these points even when the disclosure is negative.

| | |
|---|---|
| Study description | Three different iron based minerals are tested for their catalytic activity for CO2 fixation with H2 gas. |
| Research sample | Three different iron based minerals, normalized to the amount of transition metal atoms per mole. |
| Sampling strategy | We report only individual chemical experiments. The only statistics we use is to calculated the mean of various repetitions of those experiments. Each individual data point is shown additionally to the mean. |
| Data collection | MP, KI, KBM an MY collected data for product concentration (NMR, HPLC-MS, HPLC-UV, GC-FID/TCD, GC-MS) and catalyst condition (XRD, SE, TEM). MKN collected thermodynamic data via calculations of Gibbs free energy for each product under different given conditions. |
| Timing and spatial scale | Most data was collected after a reaction time of 16 hours - a time scale that was chosen to allow direct comparison between the chosen catalysts and that was shown to generate consistent results in previous publications. |
| Data exclusions | No data was excluded from the analyses. |
| Reproducibility | This manuscript is exclusively chemical, we reproduced every reported reaction at least twice, with each individual data point overlayed over the bar graph, which represents the mean. In most cases the experiments were performed in triplicate, in some cases more than than three times. Also in these cases, each individual data point is shown in addition to the mean. |
| Randomization | Not relevant. |
| Blinding | Not relevant to chemical experiments. |

Did the study involve field work? ☐ Yes ☒ No

# Reporting for specific materials, systems and methods

We require information from authors about some types of materials, experimental systems and methods used in many studies. Here, indicate whether each material, system or method listed is relevant to your study. If you are not sure if a list item applies to your research, read the appropriate section before selecting a response.

### Materials & experimental systems

| n/a | Involved in the study |
|---|---|
| ☒ | ☐ Antibodies |
| ☒ | ☐ Eukaryotic cell lines |
| ☒ | ☐ Palaeontology |
| ☒ | ☐ Animals and other organisms |
| ☒ | ☐ Human research participants |
| ☒ | ☐ Clinical data |

### Methods

| n/a | Involved in the study |
|---|---|
| ☒ | ☐ ChIP-seq |
| ☒ | ☐ Flow cytometry |
| ☒ | ☐ MRI-based neuroimaging |